Journal of
Astronomical Telescopes,
Instruments, and Systems

AstronomicalTelescopes.SPIEDigitalLibrary.org

Review of multianode microchannel array detector systems

J. Gethyn Timothy

SPIE.

J. Gethyn Timothy, "Review of multianode microchannel array detector systems," *J. Astron. Telesc. Instrum. Syst.* **2**(3), 030901 (2016), doi: 10.1117/1.JATIS.2.3.030901.

Journal of Astronomical Telescopes, Instruments, and Systems 2(3), 030901 (Jul–Sep 2016)

REVIEW

Review of multianode microchannel array detector systems

J. Gethyn Timothy*
Nightsen Inc., 294 Allandale Road, Chestnut Hill, Massachusetts 02467-3252, United States

Abstract. Multianode microchannel arrays (MAMAs) are a family of digital photon-counting imaging arrays designed specifically for use in space. Two MAMAs with formats of 1024 × 1024 pixels were included in the Space Telescope Imaging Spectrograph (STIS) to cover the far-ultraviolet (FUV) from 115 to 170 nm and the near-ultraviolet (NUV) from 165 to 310 nm. STIS was installed on orbit in the Hubble Space Telescope in February 1997. The flight-spare FUV MAMA was installed on orbit in the Advanced Camera for Surveys in March 2002, and the flight-spare NUV MAMA was installed on orbit in the Cosmic Origins Spectrograph in May 2009. This paper describes the construction, modes of operation, and on-orbit performances of the MAMAs and the resulting lessons for future space astrophysics missions. © *The Authors. Published by SPIE under a Creative Commons Attribution 3.0 Unported License. Distribution or reproduction of this work in whole or in part requires full attribution of the original publication, including its DOI.* [DOI: 10.1117/1.JATIS.2.3.030901]

Keywords: multianode microchannel arrays; ultraviolet; imaging; spectroscopy; microchannel plates; photocathodes; photon counting; photon time-tagging.

Paper 15072SSV received Sep. 8, 2015; accepted for publication Mar. 24, 2016; published online Jul. 11, 2016.

1 Introduction

Multianode microchannel arrays (MAMAs) are a family of digital photoelectric detector systems designed specifically for use in space. Development of MAMA detector systems started in the early 1970s in order to produce multielement detector arrays for use in spectrographs for solar studies on the Skylab-B mission. Two different classes of MAMA detectors have been developed, namely discrete-anode arrays and coincidence-anode arrays. Discrete-anode arrays each have pixel electrodes connected to an individual amplifier and counting circuit. This limits the total number of pixels to a few hundred because of the limitations of connector technology and the size and power requirements of the electronics.[1,2] In order to provide the 10^5 to 10^6 pixels required for astrophysics missions, coincidence-anode arrays were developed.[3] The Space Telescope Imaging Spectrograph (STIS) employs three imaging array detectors.[4] First, a back side–illuminated (1024 × 1024) pixel charge-coupled device (CCD), fabricated by Scientific Imaging Technologies, covers the visible region from ∼305 nm to the edge of the near-infrared at ∼1.0 μm. The CCD has pixel dimensions of 21×21 microns^2. Two coincidence-anode MAMAs, fabricated by the prime contractor Ball Aerospace, cover, respectively, the near-ultraviolet (NUV) and the far-ultraviolet (FUV). Each MAMA employs a single high-gain curved-channel microchannel plate (MCP) with 12-micron-diameter channels on 15-micron centers. Two readout modes are employed, as described in Sec. 2: first, low-resolution mode with 1024 × 1024 pixels having dimensions of 25×25 microns^2, and second, high-resolution mode with 2048 × 2048 pixels having dimensions of 12.5×12.5 microns^2.

Development of coincidence-anode MAMA detectors for STIS began in the late 1970s and culminated when STIS was installed on orbit in the Hubble Space Telescope (HST) in February 1997. STIS continued working until August 2004 when a low-voltage power supply failure caused observations to halt. STIS was repaired during the servicing mission in May 2009 and continues working to this day.

The flight-spare STIS FUV MAMA detector was installed on orbit in the Advanced Camera for Surveys (ACS) in March 2002, and the flight-spare STIS NUV MAMA detector was installed on orbit in the Cosmic Origins Spectrograph (COS) in May 2009. Both of these instruments continue working to this day.

The following sections of this paper describe the construction, modes of operation, and on-orbit performances of the MAMAs, and the lessons of this unprecedented period of long-term operation in space for future astrophysics missions are discussed.

2 Construction and Modes of Operation

MAMAs are a family of digital photoelectric imaging detectors. The schematic of a two-dimensional coincidence-anode MAMA is shown in Fig. 1. The core components of the MAMA are a high-gain curved-channel MCP and a precision electrode readout array to both collect and define the location of the charge from the MCP. The block diagram of the MAMA detector is shown in Fig. 2. A photocathode is mounted in proximity focus with, or deposited on, the front face of the MCP. The output charge cloud from the MCP is collected by the anode array and amplified with charge amplifiers. The decode electronics determine the location and arrival time of the charge cloud. The data are accumulated as a digital image, or the coordinates and arrival time of each photon are stored as a time-tag data stream.

2.1 *Microchannel Plates*

A conventional MCP with straight geometry channels can only provide an electron gain of 10^3 to 10^4 before the onset of significant positive-ion feedback.[5–7] Straight channel MCPs must be mounted in stacks in order to provide the electron gains of 10^5 or greater required by electronic readout systems without

---

*Address all correspondence to: J. Gethyn Timothy, E-mail: nightsen@earthlink.net

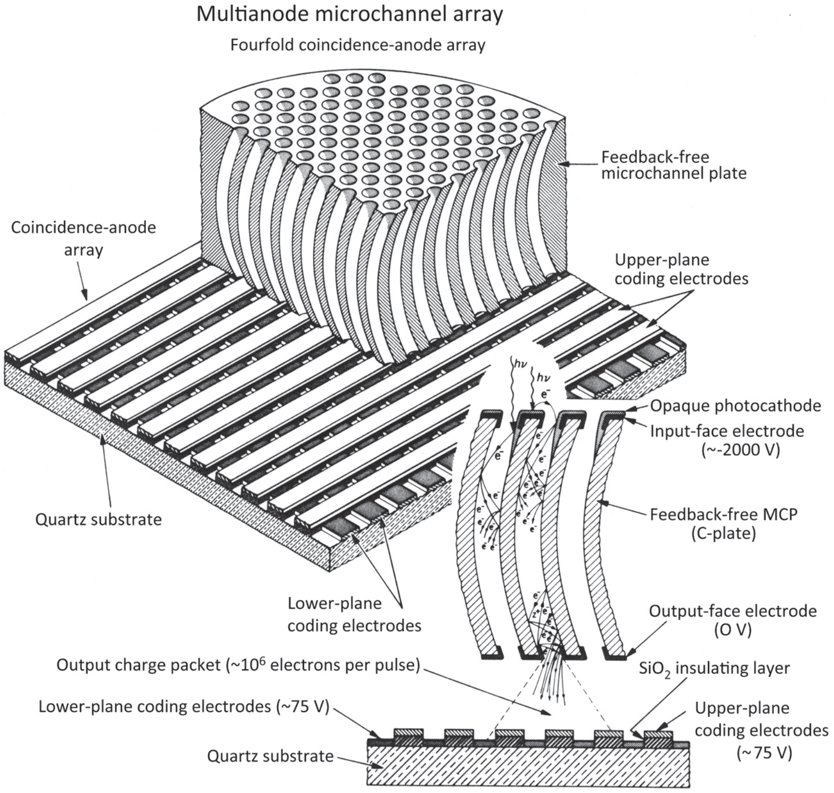

Fig. 1 Schematic of two-dimensional coincidence-anode MAMA. Typical operating voltages are shown.

positive-ion feedback. The Chevron MCP stack consists of two resistance-matched MCPs with channel bias angles on the order of 8 to 10 deg mounted in cascade, as shown in Fig. 3(a).[5]

The Z-plate MCP stack utilizes three resistance-matched MCPs mounted in cascade, as shown in Fig. 3(b).[8] In both types of stacks, positive ions are trapped at the interfaces of the MCPs. The Z-plate stack yields a better reduction of ion feedback than the Chevron stack and is the most used high-gain MCP configuration at this time. However, the Z-plate has a number of limitations when used for high spatial resolution studies. First, the unavoidable misalignments of the microchannels in the three MCPs of the stack cause strong moiré nonuniformities in the flat-field response, particularly at the multifiber boundaries.[9–11] Second, image blurring is caused by detector walk when the MCP gain changes.[12] Third, the high MCP gain required by the analog readout systems in order to precisely locate the centroid of the large output charge cloud causes significant MCP gain sag.[13] Finally, the large output charge cloud causes local gain depression in the vicinity of bright spatial or spectral features.[14]

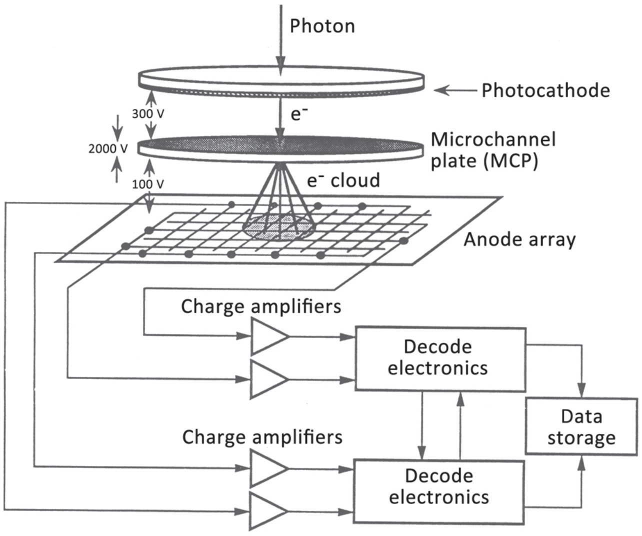

Fig. 2 Block diagram of the coincidence-anode MAMA. Typical operating voltages are shown.

The third type of high-gain MCP configuration is the curved-channel MCP or C-plate, shown in Fig. 3(c).[15] The C-plate is the only single MCP configuration that can produce electron gains of 10^5 to 10^6 without significant ion feedback. The C-plate inhibits ion feedback by curving the channels in a manner analogous to that in a conventional channel electron multiplier (CEM),[6,7] as shown in Fig. 4. Also, the modal gains of the C-plates, ranging from 10^5 to 10^6, scale in the same manner as the CEM with the channel length and the normalized channel field strength.[15] The output pulse-height distribution for a C-plate with 12-micron-diameter channels on 15-micron centers is shown in Fig. 5.[16] It should be noted that C-plates require significantly lower voltages to attain gain saturation than do either the Chevron or Z-stacks.

C-plates proved extremely difficult to fabricate, and a number of different techniques involving major efforts at a number of corporations were initiated during the Solar and Heliospheric Observatory (SOHO) and STIS programs (see, for example, Ref. 17). Other channel configurations were also tried, without success. Unfortunately, STIS schedule pressures prohibited the completion of these efforts, and no reliable and reproducible process for the fabrication of C-plates has been established to this date.

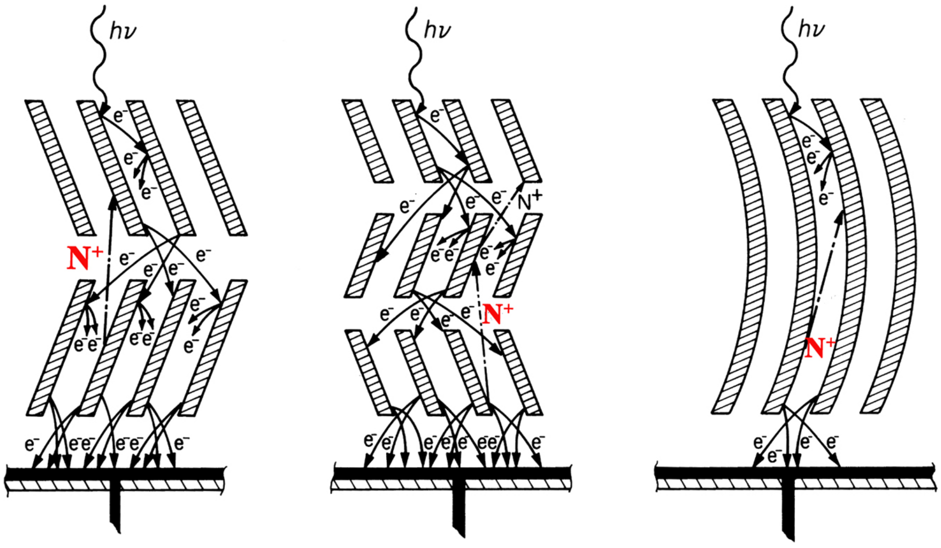

(a) (b) (c)

Fig. 3 Schematics of high-gain MCP structures: (a) Chevron MCP stack, (b) Z-plate MCP stack, and (c) C-plate MCP.

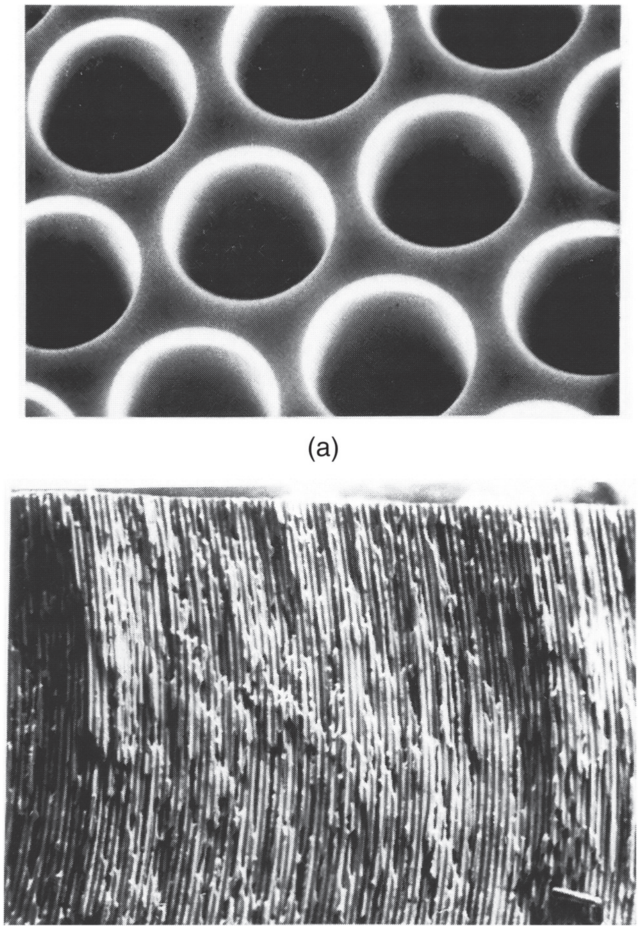

(a)

(b)

Fig. 4 C-plate with 25-micron-diameter channels on 32-micron centers: (a) face of plate and (b) section of plate.

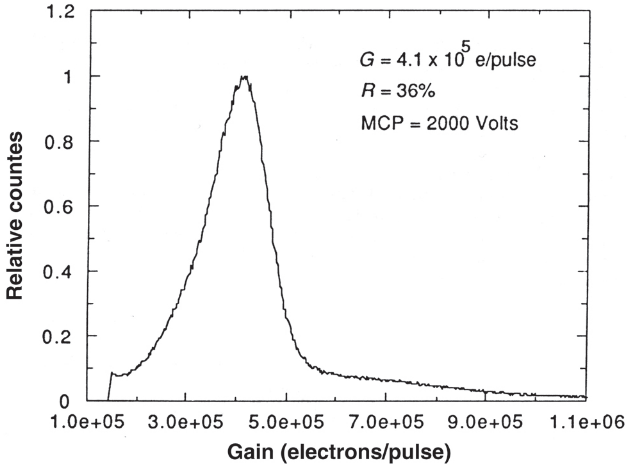

Fig. 5 Output pulse-height distribution for a C-plate with 12-micron-diameter channels.

LEP in France and Mullard in England fabricated the original C-plates.[18] Galileo Electro-Optics (now Photonis USA) started C-plate development in the United States. In addition, Litton Electron Devices (later Ni-Tec Corp.) fabricated C-plates for STIS using MCP wafers sheared by Detector Technology Inc.

In spite of these major difficulties, high-quality 25-mm-format C-plates were fabricated for the SOHO mission,[19] high-quality 40-mm-format C-plates were fabricated for STIS, and C-plates with channel diameters as small as 8 microns were fabricated for evaluation of future flight missions.[20] This was a significant achievement for both the SOHO and, particularly, the STIS development programs, allowing the C-plate technology to be successfully utilized on the STIS flight mission.

The MCPs in the Chevron and Z-plate stacks typically have channel length-to-diameter ratios on the order of 40∶1 to 60∶1.

Fig. 6 Twenty-five-mm-format and 40-mm-format C-plates.

The C-plates typically have significantly longer channel length-to-diameter ratios on the order of 100∶1 to 140∶1. This makes the C-plates thicker and more rugged than conventional MCPs. Nevertheless, two fundamental parameters of all lead-glass MCPs must be considered for all applications: (1) the very large internal surface area and (2) the negative temperature coefficient of the lead glass. The configurations of 25-mm-format and 40-mm-format C-plates are shown in Fig. 6. Thin solid rims for mounting surround the active areas, which are ∼25 and ∼40 mm in diameter, leading to outside diameters of 33 and 50 mm, respectively. The internal surface areas of the C-plates with 12-micron-diameter channels on 15-micron centers are on the order of 10^3 cm^2 to 3×10^3 cm^2. The adsorption of gas by the channel surfaces, particularly water vapor, when the MCPs are exposed to air leads to extreme pressure on the external solid rims, resulting in cracking of the plate rims. In order to prevent rim cracking, all rimmed MCPs must be stored under vacuum. Rimless MCPs are stable on exposure to air, but present problems with mounting.

This was of particular concern for the C-plates fabricated for the SOHO mission because one of the detectors for the Solar Ultraviolet Measurement of Emitted Radiation instrument was open structure, requiring the MCP to remain stable under a dry N_2 purge at atmospheric pressure for several years during instrument and spacecraft integration.

The MCP active area must be kept as small as possible in order to maximize the conductivity and hence the dynamic range. The configuration of the prototype C-plates for SOHO is shown in Fig. 7(a). Because of the concern about rim cracking, the modified flight configuration shown in Fig. 7(b) was adopted.[19] Tests in a high-humidity environment validated the structural integrity of this design. The SOHO flight configuration C-plates remained stable, while the prototype C-plates all cracked.

The STIS C-plates were used in sealed detector tubes and the SOHO configuration was not needed. Nevertheless, all of the development work with the SOHO C-plates and readout arrays was fundamental to the development of the STIS MAMAs. All of the STIS hardware was developed from the SOHO hardware, and all of the techniques and procedures developed for SOHO and all of the lessons learned from the SOHO program were utilized for STIS.

The STIS C-plates had active areas of 27×27 mm^2 to match the 1024×1024 pixel anode array (see Fig. 8).[21] This reduced the active area from that of a standard 40-mm C-plate by ∼42%, allowing a proportionally increased plate conductivity and dynamic range, but required the STIS C-plates to be maintained at all times in a hydrocarbon-free high-vacuum environment.

All of the lead-glass MCPs have negative temperature coefficients of resistance. Because of the very large internal surface area, it is necessary to bake and scrub the MCPs before a stable operating regime is reached. The MCPs were baked in a hydrocarbon-free environment at a temperature of typically 300°C for a period in excess of 24 h. During the bake, the outgassing of the MCP was recorded on a residual gas analyzer, and the MCP resistance was measured during the heating and cooling cycles. The resistances as functions of temperature for Mullard glass and Galileo Long Life™ glass C-plates are shown in Fig. 9. The ohmic heating of the MCP during operation increases both the operating temperature and the operating current. If the resistance is too low, the positive feedback of the ohmic heating leads to thermal runaway and the destruction of the plate. The SOHO C-plates fabricated from Long Life™ glass had active areas of ∼270 mm^2 and resistances in the range of 24 to 44 MΩ. The average operating temperatures in an ambient environment of 20°C lay in the range of 60 to 75°C. The STIS C-plates fabricated from 8161 glass had active areas of ∼730 mm^2 and resistances in the range of 25 to 54 MΩ.[22] The STIS C-plate operating temperatures were typically in the range of 14 to 21°C above the ambient temperature.

The modal gain of the Long Life™ glass C-plates decreased with increasing temperature at a rate of $-0.1\%\ (^\circ\mathrm{C})^{-1}$. This was attributed primarily to an axial temperature gradient along the MCP, creating a nonuniform electric field within the channel that lowers the effective output gain.[22] The same effect caused the modal gain of the 8161 glass STIS C-plates to decrease with increasing temperature at a rate of $-0.14\%\ (^\circ\mathrm{C})^{-1}$. These gain changes with temperature had a negligible effect on the STIS detective quantum efficiency (DQE).[23]

The scrub of the MCP is carried out after baking in the same detector tube under a hydrocarbon-free high-vacuum environment without exposure to air. Rugged discrete-anode arrays are used for the scrub and characterization of the C-plates, as shown in Fig. 10. The curvature of the channels in the C-plate inhibits the motion of neutral particles as well as positive ions. The scrub of the channels must accordingly be undertaken at a rate that does not lead to an excessively high pressure in the channels. A mercury Pen-ray light source is used to stimulate the bare MCP with 2537 Å radiation. The C-plate scrub is started at the applied potential where output counts start to be observed above the charge amplifier/discriminator threshold, typically ∼1400 to 1500 V.

The applied potential and the signal level are gradually increased over a period of about two weeks or longer until the final operating voltage is reached. This is typically in the range of 2000 to 2200 V. The total charge extracted from the C-plate during scrub lies in the range of 0.5 to 1.5 C cm^{-2}. The operating characteristics then remain stable until a further 1.5 C cm^{-2} or greater of charge is extracted from the C-plate.[15,23] This was significantly in excess of the 0.5 to 1.0 C cm^{-2} of charge expected to be drawn from the C-plates during the planned five-year mission of STIS.[24] In fact, the C-plates have so far remained completely stable during the nearly 14.5 years of STIS on-orbit operation.

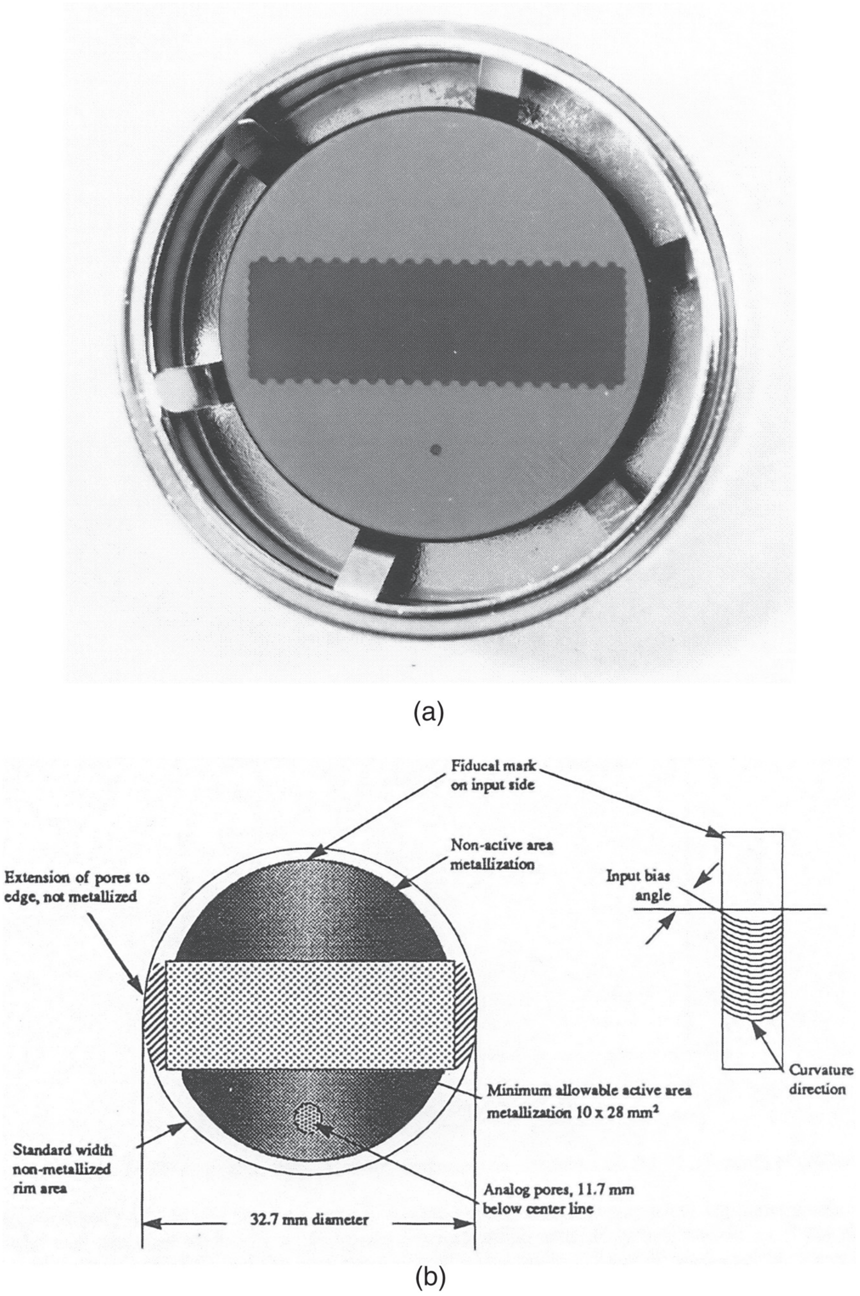

Fig. 7 SOHO C-plate configurations: (a) prototype 25-mm-format C-plate with $7 \times 27\ \text{mm}^2$ active area and (b) flight configuration.

2.2 *Coincidence-Anode Arrays*

The very small dimensions of the channels in the MCP result in a very short electron transit time and transit time jitter. The output pulse width of a conventional discrete-dynode electron multiplier is on the order of 30 to 50 ns with a rise time on the order of 6 to 10 ns. By comparison, the pulse width of a C-plate with 12-micron-diameter channels is on the order of 2 to 3 ns with a rise time on the order of 400 to 500 ps.[25] Consequently, the coincidence-anode arrays, the electrode structures of the detector tubes, and the electronics are all extremely sensitive to capacitive and inductive coupling. As a result, three different coincidence-anode array formats were developed, as shown in Fig. 11.[3] In the coarse-fine and balanced-coarse-fine arrays [Figs. 11(a) and 11(b)], $2(n+m)$ outputs encode $(n \times m)^2$ pixels in a two-dimensional array. The coarse- and fine-encoding electrodes are capacitively balanced but inductively coupled. There is also a position ambiguity for fourfold and higher-fold events in each axis. In the fine-fine array [Fig. 11(c)], $4(n+1)$ outputs encode $[n \times (n+2)]^2$ pixels in a two-dimensional array. There is no position ambiguity for up to $(n-1)$-fold events in each axis. The number n must be even to avoid position ambiguities in the last group of electrodes in each axis. All electrodes are capacitively balanced and inductively decoupled.

The unique position accuracy and the flat-field uniformity, limited solely by the photon statistics, for the fine-fine arrays were validated in a series of laboratory evaluations.[26,27]

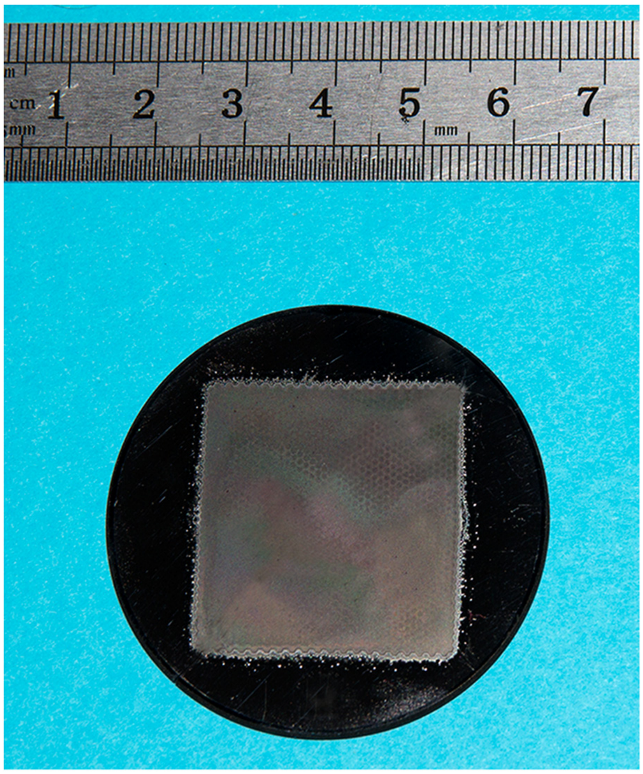

Fig. 8 STIS C-plate configuration.

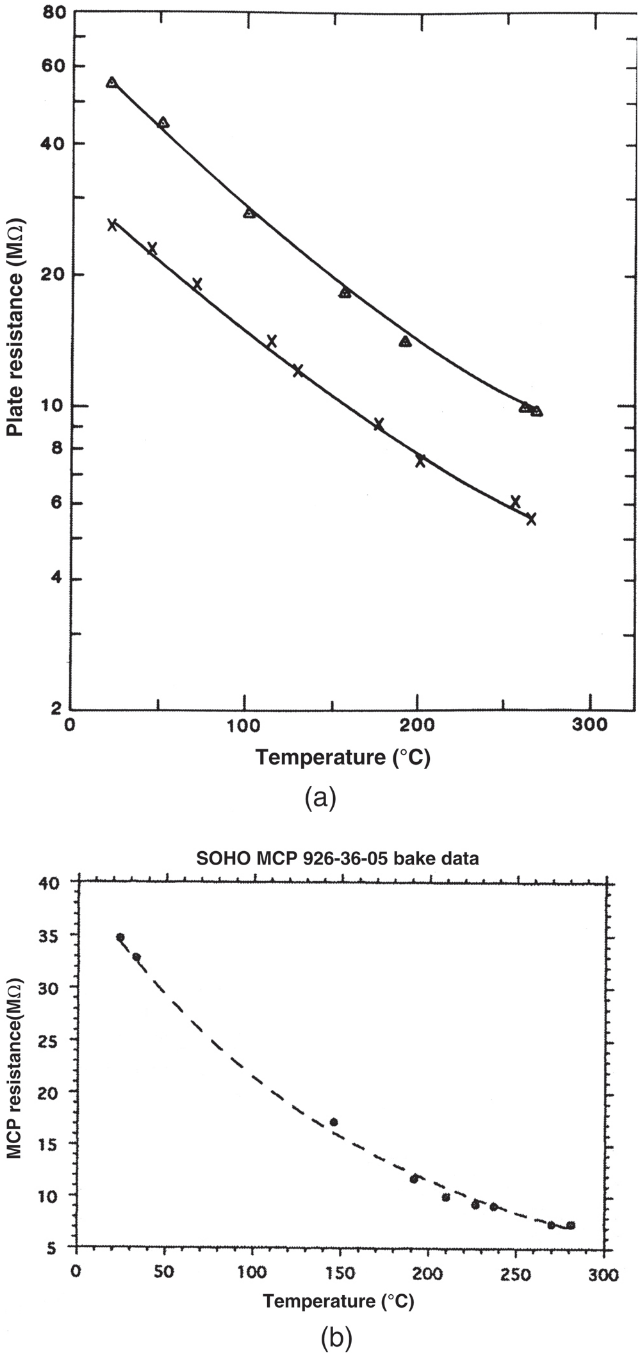

Fig. 9 C-plate resistances as functions of temperature: (a) Mullard 25-micron-diameter channels and (b) Galileo Long Life™ 12-micron-diameter channels.

The schematic of one axis of a fine-fine array is shown in Fig. 12. It can be seen that a fourfold event can be defined as an equivalent twofold event, thereby preserving the inherent spatial resolution. In a standard coincidence-anode MAMA, the pixel size is equal to the spacing of the anodes, which is 25 microns for STIS. However, it is possible to increase the resolution of the MAMA without changing the detector itself by simply upgrading the readout electronics. Using the odd-even discrimination to differentiate between the even-fold and odd-fold events, it is possible to halve the pixel spacing and double the number of pixels in each axis, as shown in Fig. 13.[28] The spacing of the channels in the MCP then sets the spatial resolution, which is 15 microns for STIS. It must be noted that odd-even discrimination works only for the C-plate and does not work for the Chevron or Z-plate stacks because of the misalignments of the channels in the different MCPs in the stack.

During operation of the fine-fine array, the statistical distribution of the anode fold numbers provides information on the distribution of the charge cloud sizes on the anodes. This fold analysis measurement[29] provides a good indication of the pulse-height distribution of the MCP as charge is extracted during operation (see Sec. 3) and is an excellent monitor of the health of the MAMA detector.

When NASA originally selected STIS for development in November 1985, two fine-fine coincidence-anode MAMA detectors with formats of 2048 × 2048 pixels were selected for the FUV and NUV spectral regions. However, the development of STIS was severely impacted by two significant events: (1) the loss of the space shuttle Challenger in February 1986 and (2) the discovery of the spherical aberration in the HST primary mirror after launch in April 1990. The spherical aberration problem forced the installation of STIS to be deferred to the second HST servicing mission (SM2), allowing the corrective optics package (COSTAR) to be installed in the HST on the first servicing mission (SM1). In March 1991, STIS was descoped in response to budget problems within the HST project. After descope, STIS incorporated two fine-fine MAMA detectors with formats of 1024 × 1024 pixels. NASA accepted this configuration of STIS in October 1991.

Raytheon Corp fabricated the first coincidence-anode arrays with aluminum electrodes. Aluminum provides excellent uniformity, high conductivity, and excellent adhesion to the dielectric substrate. Unfortunately, the aluminum arrays developed shorts when baked to temperatures in excess of 200°C because

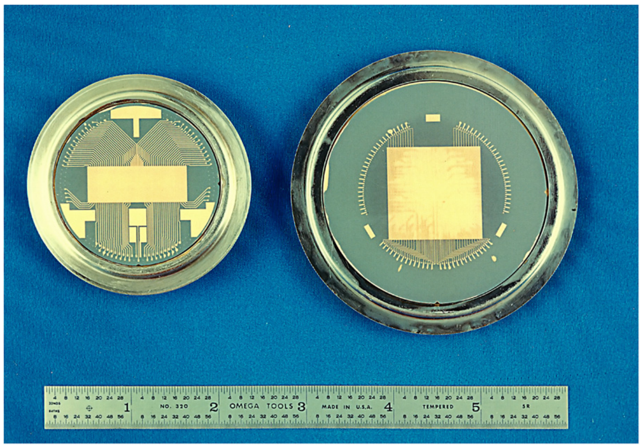

Fig. 10 Discrete-anode arrays for scrub and characterization of MCPs: (a) 1 × 160 array for 25-mm-format MCPs with 7×27 mm^2 active areas and (b) 1 × 100 array for 40-mm-format MCPs with 27×27 mm^2 active areas.

of dendritic growth. When the array fabrication was moved to Ball Aerospace, the electrode material was changed to titanium-tungsten-gold. This eliminated the dendritic growth and further improved the electrode conductivity.

The pre-descope (2048 × 2048)-pixel coincidence-anode array (see Fig. 14) was configured as four contiguous and independent (1024 × 1024)-pixel arrays.

This array format was included in a 75-mm-format tube (see Sec. 2.3). One section was evaluated and worked exactly as expected.

When STIS was descoped, one quarter of this array was selected for flight, as shown in Fig. 15. For the flight MAMAs, the encoding electrodes were arranged on all four sides of the active area of the array in order to further minimize the capacitative coupling.

Photomicrographs of the active area of this array (Fig. 16) show that the lower-plane electrodes (horizontal) are thicker than the upper-plane electrodes (vertical) in order to ensure that the charge division between the layers is more uniform. The

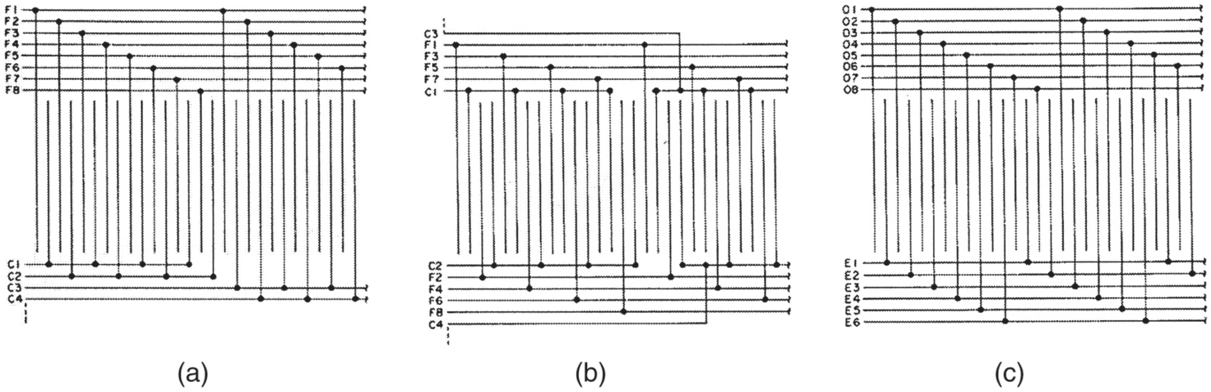

Fig. 11 One-dimensional schematics of coincidence-anode array configurations: (a) coarse-fine array, (b) balanced coarse-fine array, and (c) fine-fine array.

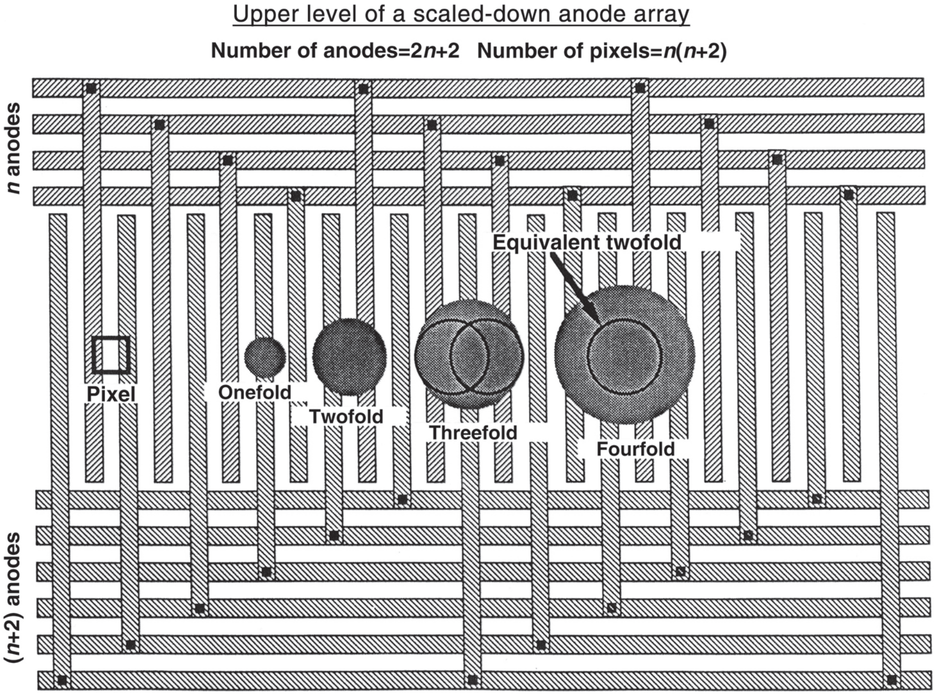

Fig. 12 Schematic of one axis of a fine-fine anode array with multifold events.

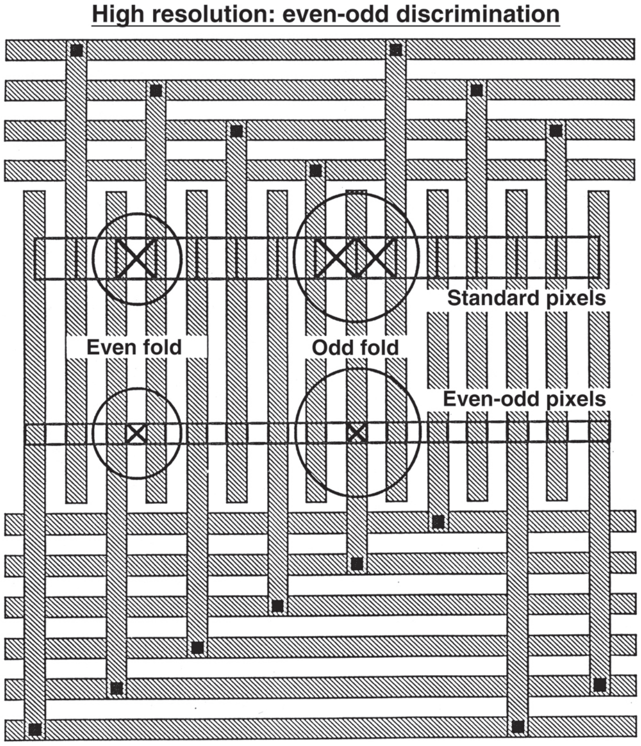

Fig. 13 High-resolution decode mode with odd-even discrimination.

center-to-center spacing of the electrodes is 25 microns. The two layers are separated by ~3 microns of dielectric in order to reduce the capacitive coupling. The anode electrodes are set at a potential of ~150 V more positive than that of the output face of the MCP in order to optimize the collection of charge from the MCP. The division of charge between the layers was totally equalized by setting the bias of the lower electrodes about 1 to 2 V more positive than that of the upper electrodes. The width of the electrodes is ~12.5 microns and the total length of the electrodes in the array is ~52 m. The total number of electrode crossovers is $>10^6$. The fact that a number of arrays were fabricated defect-free (no breaks or shorts) is a tribute to the skill of the personnel and the quality of the facilities at Ball Aerospace.

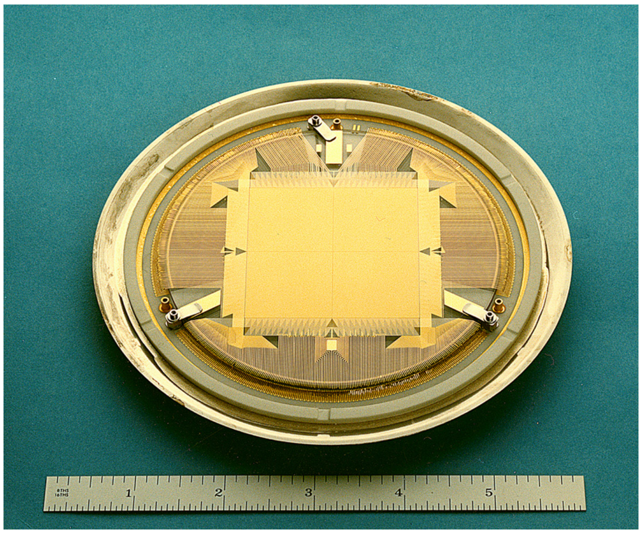

Fig. 14 A (2048 × 2048)-pixel fine-fine coincidence-anode array.

Fig. 15 STIS (1024 × 1024)-pixel coincidence-anode array (courtesy Ball Aerospace).

2.3 *Photocathodes and Detector Tubes*

It is essential that both of the STIS MAMA detectors be blind to visible light. The best solar-blind photocathode materials for use at extreme UV and FUV wavelengths are alkali halides directly deposited on the front face of the MCP.[30,31] In the MAMA tubes, a focusing electrode is used to redirect electrons formed from photons striking the web surface between the channels into the adjacent channels,[3] thereby increasing the DQE. MAMA detector tubes were constructed for the 25-, 40-, and 75-mm-format C-plates. The STIS FUV MAMA tube schematic is shown in Fig. 17.[32] The MgF_2 input window is tilted in order to accommodate the input beams from the STIS optics, and an additional

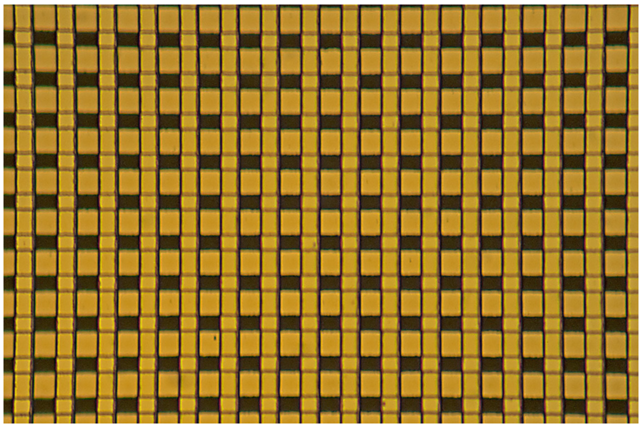

Fig. 16 Photomicrograph of a section of the active area of an STIS anode array. Electrode center-to-center spacing is 25 microns.

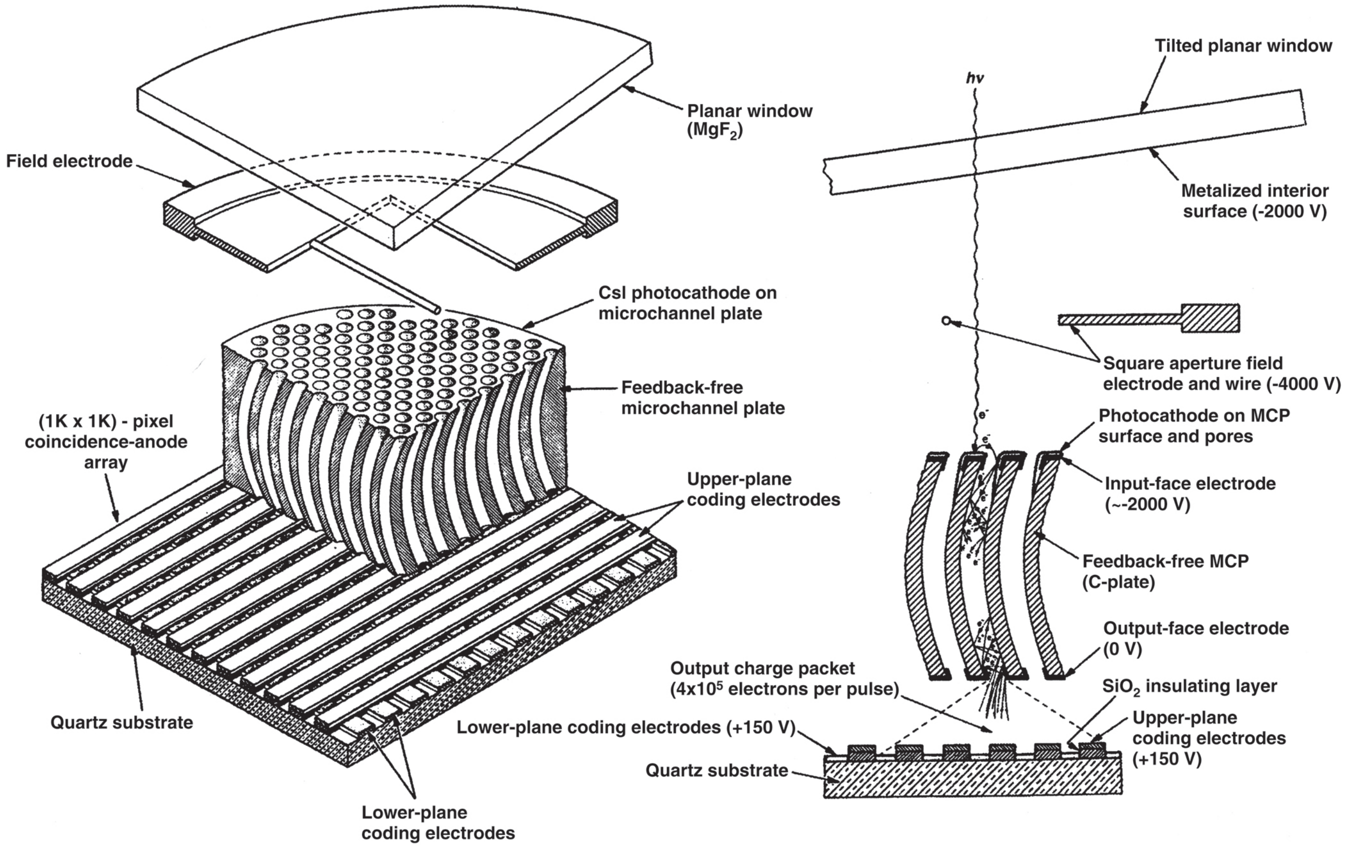

Fig. 17 Schematic of the STIS FUV MAMA detector tube (courtesy STScI, from Ref. 32).

repeller wire is used to ensure the uniformity of the photoelectron collection across the active area of the MCP. An opaque CsI photocathode is deposited on the front face of the C-plate in order to provide the optimum DQE for the FUV band from 115 to 175 nm.

Since CsI is hygroscopic in nature, the key to maximizing the DQE is to ensure that the photocathode is always maintained under high vacuum. This was achieved for the STIS MAMAs by sealing the tube window after photocathode deposition before the tube was exposed to air.

For wavelengths longer than ~200 nm, cesiated photocathodes must be employed.[33] The best material for the NUV band from 165 to 310 nm is Cs_2Te. This cathode is fabricated by depositing tellurium in a cesium-rich atmosphere. The problem is that the cesium vapor poisons the MCP. The solution is to remotely deposit, in a separate vacuum chamber, the Cs_2Te on a window to form a semitransparent photocathode. The window is then transferred under vacuum and bonded to the flight MAMA tube. The structure of the STIS NUV tube is shown in Fig. 18.[32]

A reentrant MgF_2 window is employed to limit the gap between the semitransparent photocathode and the input face of the C-plate to ~0.23 mm in order to maintain the required spatial resolution of 25 microns. The MAMA tube processing consisted of a 12-h vacuum bake at 300°C and a four-week MCP scrub. CsI photocathode deposition occurred at the end of the MCP scrub, while the Cs_2Te photocathode deposition was performed prior to the MCP scrub in order to remove excess photocathode constituents from the MCP. The DQEs of the FUV and NUV STIS MAMAs are shown in Fig. 19. The vacuum chamber pressures were maintained below 10^{-9} Torr at all times. The DQE of the FUV MAMA exceeds the performance specification by a factor of 1.4. Further, the NUV MAMA has a sufficiently high DQE below ~160 nm to provide an efficient backup to the FUV MAMA. Both detectors demonstrated visible light rejections that were better than required.[34]

2.4 *Electronics*

The electronics for the STIS MAMAs were developed in stages. A number of discrete-component systems were designed and fabricated at Ball Aerospace for use on the ground and in sounding rockets.[35] A typical discrete-component system is shown in Fig. 20. It was clear that in order to meet the power, volume, and mass requirements for SOHO and for STIS, application-specific integrated circuits (ASICs) would need to be developed for both the amplifier/discriminator and decode circuits. The first amplifier/discriminator ASICs for SOHO were developed at Ball Aerospace, resulting in the more compact configuration shown in Fig. 21.[35,36] The high-gain bandwidth circuits required great care with both components and layouts in order to minimize cross-coupling and timing errors. In particular, while both amplifier and discriminator circuits were fabricated in the same circuit module, separate modules were used in series, first for the amplifier and second for the discriminator (see Fig. 22). The ASIC amplifiers and discriminators for STIS were further refined from the SOHO modules.[37,38]

The amplifier speed was increased, and both the noise and power were reduced. In particular, the discriminator thresholds were matched in order to improve the flat-field uniformity of

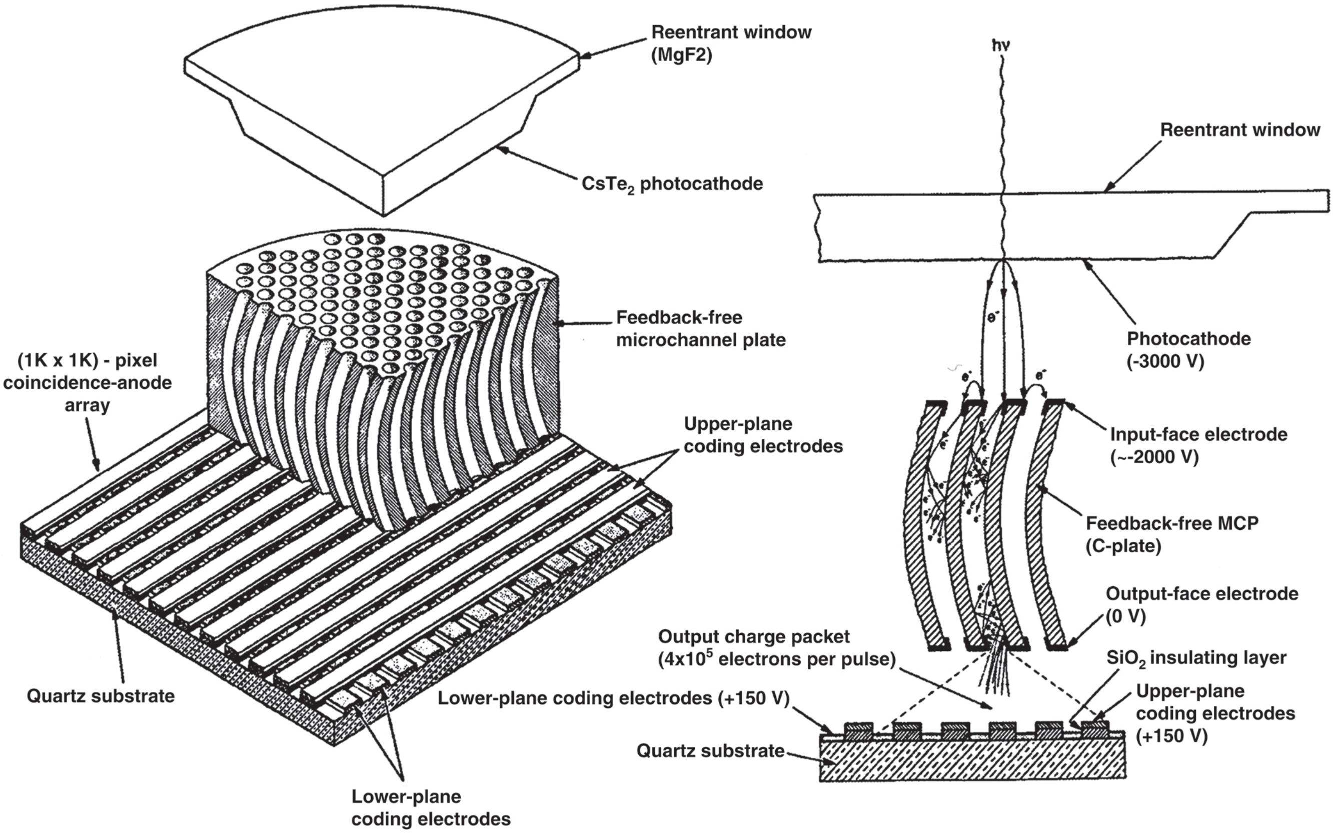

Fig. 18 Schematic of the STIS NUV MAMA detector tube (courtesy STScI, from Ref. 32).

response. A single ASIC was used for each amplifier circuit, and two discriminator circuits were packed in a single ASIC. Ten channels were mounted on each amplifier and discriminator board.[39]

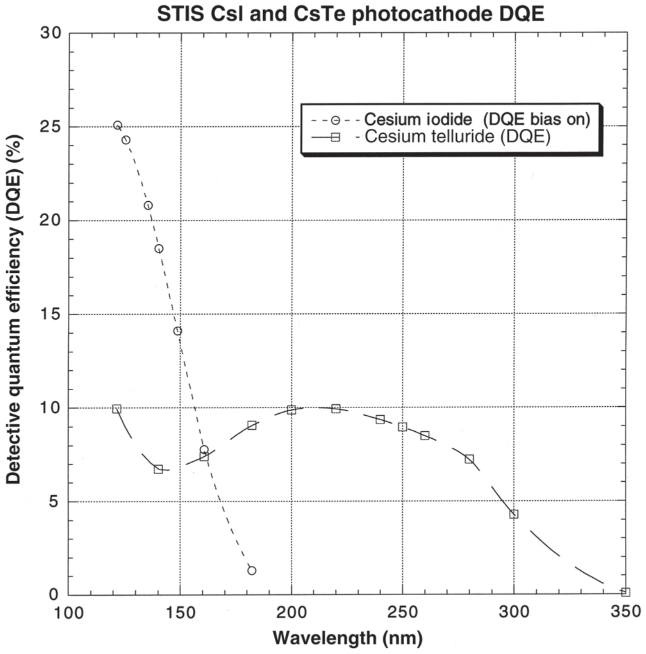

Fig. 19 STIS FUV and NUV MAMA detective quantum efficiencies.

In parallel with the amplifier/discriminator ASIC development at Ball Aerospace, the development of a complementary metal-oxide semiconductor (CMOS) decode circuit ASIC was undertaken at Stanford University.[40,41] This ASIC (see Fig. 23) was designed to optimize both the time-tag imaging[42,43] and the high-resolution decoding[28] of the MAMA detectors. The ASIC also provided information on the number of anodes stimulated by a single event. This information (fold analysis) provides a measure of the electron gain and the health of the MAMA detector tube, as described in Sec. 3. The ASIC was designed

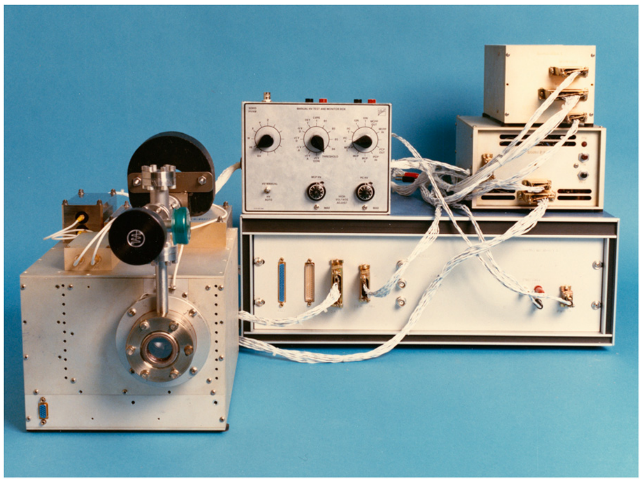

Fig. 20 Typical discrete-component MAMA detector system.

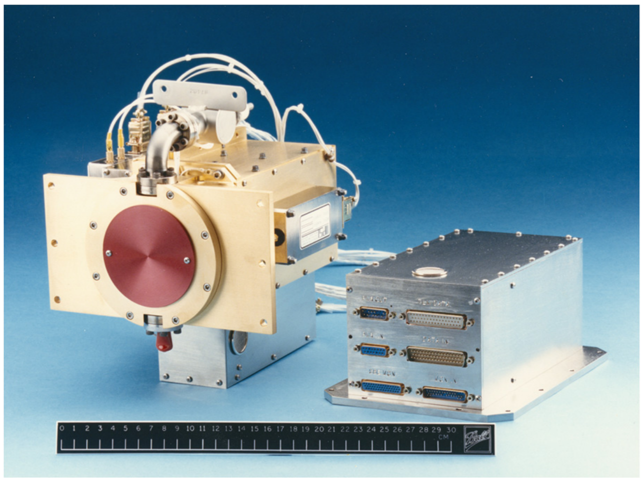

Fig. 21 First ASIC MAMA detector system.

to provide measurements of the number of twofold through sixfold events. In addition, the ASIC rejected single events, events greater than sixfold, and events on noncontiguous anodes. This is particularly valuable in rejecting Cherenkov photons produced essentially simultaneously by the passage of energetic charged particles through the detector windows when operated in space.

The time-tag imaging and high-resolution decoding capabilities led to a multiyear program of speckle observations of binary stars[44] at both Kitt Peak, Arizona and South America.[45,46] The fact that the visible-light MAMA detector with 14-micron pixels was used by many individuals at several different locations over a number of years without any problems testifies to the inherent ruggedness of the detector system. Further, the time-tag imaging mode of the MAMA was used to correct the pointing drift of a gyro-stabilized sounding rocket.[47] This permitted the recording of an image with sufficiently high angular resolution to directly measure the UV luminosity.[48] The basic properties of the MAMAs were thus fully validated on the ground, both for the SOHO and speckle image programs, and in a sounding rocket, before the fabrication of the STIS engineering model and flight MAMAs began.

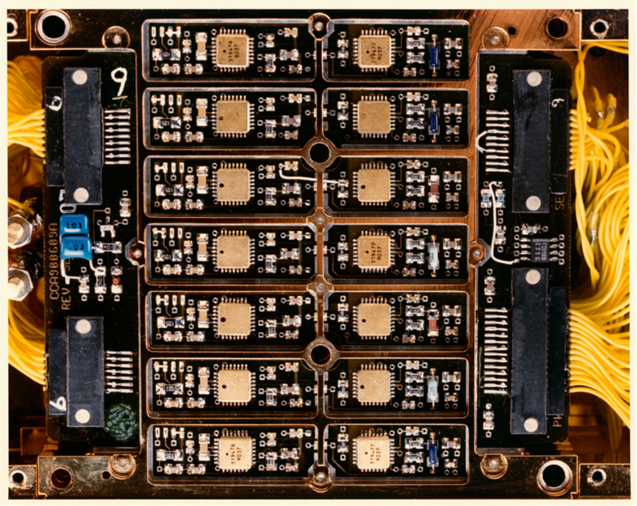

Fig. 22 SOHO amplifier and discriminator ASICs mounted in series in a seven-channel module.

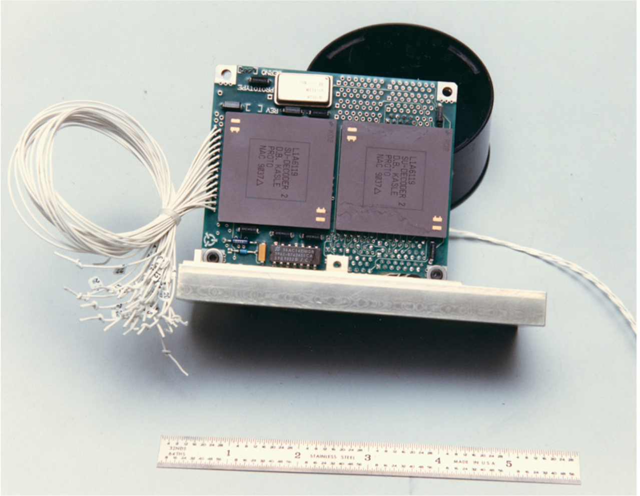

Fig. 23 Decode ASICs for a two-dimensional MAMA (one ASIC for each axis).

2.5 *Prelaunch Performance Summary*

A number of complete engineering models of the STIS MAMAs were fabricated in 1994 (see Fig. 24) and were subjected to a series of exhaustive tests and evaluations.[49] In particular, the photometric stability was analyzed in detail at the component level.[50] Of particular importance was the fact that significant overload of the detector by an image many times brighter than the local dynamic range produced no residual effect after the image was removed.[24] This fully confirmed earlier results with the ground-based MAMA detector systems.

The critical parameters of the MAMA detectors leading to the excellent performance characteristics and long lifetime are the single C-plate with a modal gain of $\sim 5 \times 10^5$ electrons pulse^{-1}, low-noise amplifier/discriminator circuits with a threshold of 2.74×10^4 electrons, a high-precision fine-structure readout array, and a digital position encoding system.

It should be clearly noted that, given the total charge lifetime of the lead-glass MCP, a readout system that requires a gain of only 5×10^5 electrons pulse^{-1} will have a total count lifetime about a factor of 100 greater than that of a readout system that requires a gain of 5×10^7 electrons pulse^{-1}. Further, given the

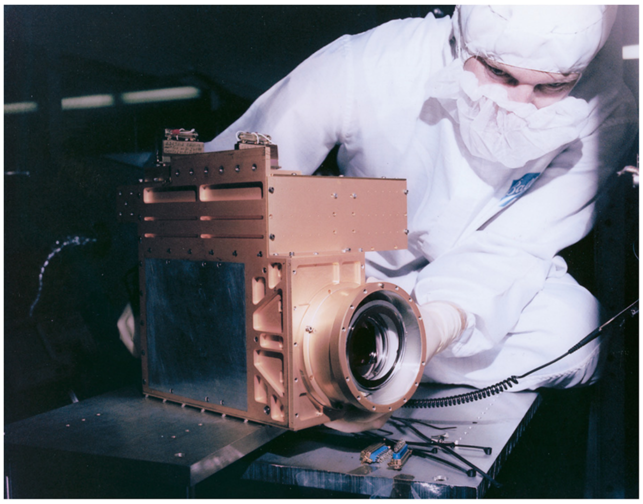

Fig. 24 Engineering model of the STIS NUV MAMA detector (courtesy Ball Aerospace).

Table 1 Key performance characteristics of the STIS MAMA detectors.[51]

	FUV MAMA	NUV MAMA
Wavelength range	115–170 nm	165–310 nm (prime)
		115–170 nm (backup)
Low-resolution pixel size	25×25 microns^2	25×25 microns^2
Spatial resolution (FWHM) (with high-resolution readout)	22.7 microns	29.3 microns
Quantum efficiency	~21% (142 nm)	~9.5% (237 nm)
Dark count rate (low resolution pixel)	$5 - 10 \times 10^{-6}$ counts pixel^{-1} s^{-1}	$0.6 - 1.5 \times 10^{-3}$ counts pixel^{-1} s^{-1}
Dynamic range (10% rolloff)		
Local (MCP limited)	220 counts pixel^{-1} s^{-1}	340 counts pixel^{-1} s^{-1}
Global (electronics limited)	3.05×10^5 counts pixel^{-1} s^{-1}	3.05×10^5 counts pixel^{-1} s^{-1}
(low resolution pixel)		
Flat field uniformity (low resolution pixels)	6.4% rms	3.1% rms
Flat field stability (changes in 2×2 low-res pixels)	over 4 months	over 21 days
	<1%rms	<0.68%rms
Visible-light rejection (QE at 400 nm)	1.5×10^{-10}	2.7×10^{-4}

total charge throughput of the MCP (~10% of the strip current), the total output count capability will be significantly greater.

The key performance characteristics of the STIS MAMAs are listed in Table 1 (from Ref. 51). All of the data, except for the dark count rate, are from ground calibrations. The FUV and NUV MAMAs were fabricated as mirror images in order to permit the detector tubes to lie adjacent to each other on the STIS optical bench [see Fig. 25(a)].[50] One flight and one flight spare unit of both the FUV and NUV MAMA detectors were fabricated and calibrated, as shown in Fig. 25(b).

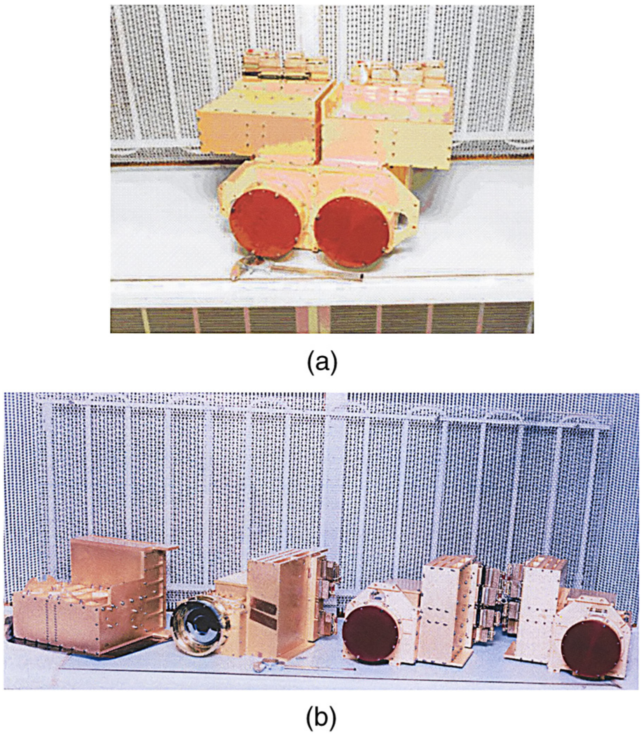
(a)

(b)

Fig. 25 Flight MAMA detectors: (a) STIS flight FUV and NUV MAMAs and (b) flight and flight-spare FUV and NUV MAMAs (courtesy Ball Aerospace).

3 On-Orbit Performances

3.1 *Space Telescope Imaging Spectrograph Initial Operation*

STIS was installed on orbit on the second Hubble servicing mission (SM2) in February 1997. As with earlier instruments utilizing high voltages, the MAMAs were brought into operation cautiously over a period of several weeks in the somewhat unknown internal environment of the HST.

Two unexpected issues emerged on initial turn on. First, the reset circuitry in the control electronics for both the MAMA and CCD detectors showed an unforeseen response to radiation-induced transients in the optical isolator components in the electronics chain.[52,53] Energetic particles [encountered primarily in the South Atlantic Anomaly (SAA)] caused a partial reset of the detector electronics, abruptly shutting down the MAMA high voltage. This requires the MAMA high voltages to be ramped up and down at the normal slow rate once per day in the block of contiguous paths that do not cross the SAA. This restricts the MAMA availability to 40 to 45% of HST orbits, adequate for the planned MAMA science. No adverse effects of the daily voltage recycling have so far been observed. The problem is totally unrelated to the MAMA design and has been corrected for ACS and COS, which are using the flight-spare STIS MAMAs.

The second unexpected problem is the high dark count rates of the MAMAs. The FUV MAMA dark count rate was known to correlate with temperature, and the on-orbit rate varies from the preflight rate of ~6 to ~50 counts s^{-1} depending on the MAMA temperature.[32,52] The enhanced dark background is not spatially uniform but localized on the detector, as shown in Fig. 26. The dark current in lower right-hand quadrant appears to be roughly stable with time, while the intermittent dark count rate in the glow area, which is intrinsic to the C-plate, varies with time and can increase the dark count rate over the face of the MAMA up to 300 counts s^{-1}.

The significantly higher than expected background rate of the NUV MAMA is a more serious problem. It was well known that longtime constant phosphorescence in the MgF_2 window would occur after the excitation of metastable states during the SAA crossings. The phosphorescent de-excitation of these states produces UV photons that are detected by the MAMA. A preflight screening program for phosphorescence was used for the MAMA detector windows. Unfortunately, an error in the screening allowed a window with a high level of phosphorescent impurities to be used in the flight NUV tube. While the dark count of the NUV MAMA is spatially more uniform than that of the FUV MAMA, the high rate on the order of 1000 to 2000 counts s^{-1} makes it more problematic for long-exposure studies.[52]

STIS was designed as a highly versatile imaging spectrograph providing major advances on both the Goddard High-Resolution Spectrograph and the Faint Object Spectrograph through the use of two-dimensional detector arrays. It was essential that STIS have a high signal-to-noise ratio (SNR) for all studies. A series of studies of the SNR in a number of operating modes were undertaken during the first few months of operation.[54] FUV and NUV flat-field images were recorded during these studies (see Ref. 54). The NUV flat fields were verified to be independent of wavelength and operating mode. FUV flat fields also showed no wavelength dependence. However, there was a small residual effect in removing an overall moiré pattern from the flat fields, which was more pronounced in the FUV flat field (≤6% peak-to-peak) than in the NUV flat field.[54] The results for the MAMAs were highly encouraging with both long-slit low-resolution first-order spectra and medium-resolution echelle spectra yielding SNRs well exceeding 100∶1 per spectral resolution element in both the NUV and FUV. Even higher SNRs were obtained using multiple slits offset from each other by a total of 0.5 arc sec along the dispersion direction (FP-SPLIT method).[55] Co-added spectra exhibited an SNR of ~250 in the FUV and ~350 in the NUV per spectral resolution element.

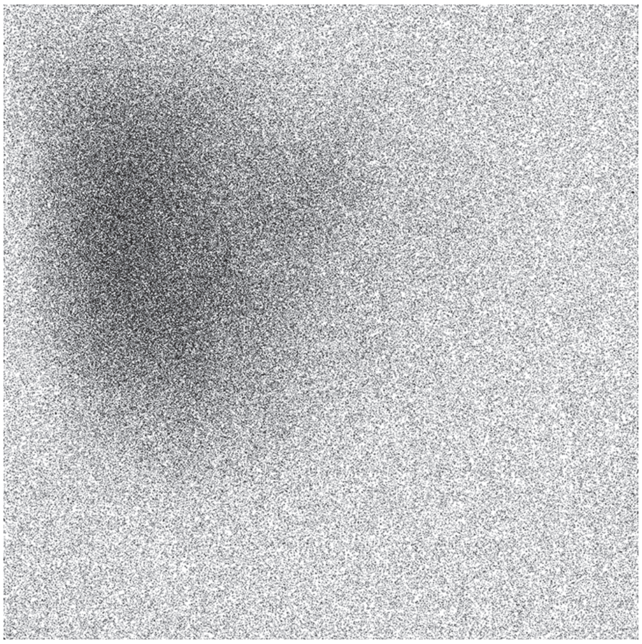

Fig. 26 STIS FUV MAMA dark map (courtesy STScI, from Ref. 32).

A further essential monitor of MAMA performances is the fold analysis measurement[29] as discussed earlier in Sec. 2. Examples of fold analyses for the FUV and NUV MAMAs are shown in Fig. 27. Fold analyses during the first year of on-orbit operation showed good tube health and very high MCP gain stability,[29] essentially unchanged from the preflight measurements.

The three primary operating modes of the STIS MAMAs are (1) solar-blind UV imaging, (2) stigmatic low- and high-resolution UV spectroscopy, and (3) time-tag UV imaging and spectroscopy. As an example of solar-blind imaging, an image of Saturn's UV aurora is shown in Fig. 28.[56] All of the MAMA imaging and spectrometry data were recorded in high-resolution mode (ACCUM), i.e., in the (2048 × 2048)-pixel format. The power of the two-dimensional MAMAs for spectroscopy is shown in the echelle spectrum in Fig. 29.[57] Resolving powers ($\lambda/\Delta\lambda$) of $>10^5$ were routinely obtained.[58] The unique capabilities of the MAMAs for time-tag imaging are shown in the Crub pulsar profile spectra as a function of pulse phase in Fig. 30.[59]

In all respects, except for the dark count rates, the STIS MAMAs met all of the preflight performance requirements.

3.2 *Space Telescope Imaging Spectrograph Recovery*

STIS worked well on orbit from February 1997 until 16 May, 2001, when the main power bus blew a fuse.[60] Attempts to recover resulted in another blown fuse, and detailed engineering analyses concluded that the most likely cause was a shorted tantalum capacitor. It was concluded that the side-1 electronics could never be recovered. On July 7, 2001, the redundant side-2 electronics was successfully used to reactivate STIS. Although the operation of the CCD was affected by the lack of a temperature sensor in the side-2 electronics, the MAMAs and the rest of the electronics continued operating unaffected.[60] STIS operations continued until August 3, 2004, when a 5-V power converter failed.[61] All of the detectors were undamaged, but since this power converter was required for the operation of all of STIS mechanical moving parts, science operations could no longer continue. The only solution was to replace the side-2 electronics board containing the failed power converter.

On February 1, 2003, the space shuttle Columbia was destroyed on reentry. As with the loss of Challenger, this resulted in a delay of over two years to the shuttle program. Further, NASA decreed that all future shuttle missions would go to the International Space Station, which could act as a lifeboat in case of emergency. However, on October 31, 2006, NASA administrator Michael Griffin announced one final HST servicing mission (SM4). Following this decision, Ball Aerospace designed an upgraded 5-V power converter and modified the associated electronics board, and NASA, Ball Aerospace, and the Space Telescope Science Institute (STScI)

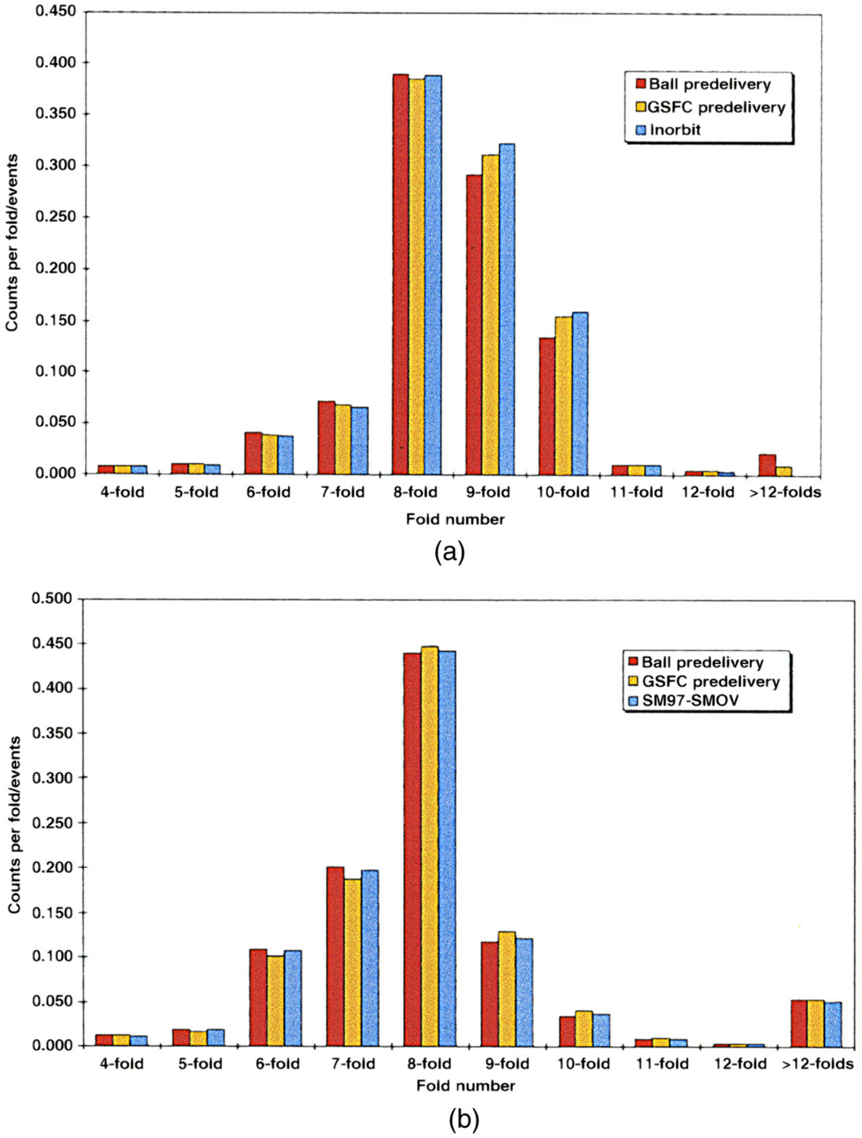

Fig. 27 (a) STIS FUV and (b) NUV MAMA fold analyses preflight and on-orbit (courtesy H. Ferguson et al., from Ref. 29).

worked on procedures for the on-orbit replacement of the side-2 circuit board containing the 5-V power converter.[61]

Since SM4 was scheduled for 2007 at the earliest, there was concern over the recovery of the MAMAs after more than four years of nonoperation on orbit. In fact, SM4 did not take place until May 2009. Through 2007 and 2008, the author supported a group of individuals from NASA Goddard and STScI who were studying the problem. The principal concern was that free cesium from the photocathodes could have migrated into the C-plate channels and caused shorts or arcing when the MCP high voltage was applied. The concern was greatest for the NUV MAMA with the semitransparent Cs_2Te photocathode.

The key to the solution of the problem lay in the thermal time constant of the C-plates. Both C-plates require over 11 min to come to a stable operating temperature. The procedure adopted was to bring the MCP high voltage on in stages, working with one MAMA at a time, then holding the voltage at a stable level while measuring the dark count rate and performing a fold analysis. The high voltage was first brought up to ~50 V, then slowly in stages up to a voltage of ~100 V below the nominal. After careful analysis of both the dark count rate and fold distribution, the high voltage would then, if all looked to be well, be brought to the normal operating level.

During SM4, on the fourth extravehicular activity, astronauts Michael Good and Mike Massimo successfully replaced the failed circuit board and STIS was returned to operation after nearly six years of nonoperation on orbit.[62] After an adequate period for outgassing, both MAMAs were successfully turned on following the developed procedure. Initially, it was thought that the DQEs had declined, but this was due to the fading of the STIS wavelength calibration lamps. The biggest surprise was the very high dark count rate of the NUV MAMA. It was expected that the dark count rate would be enhanced by a factor of ~3 above the pre-SM4 level of ~0.0013 counts $\text{pixel}^{-1}\ \text{s}^{-1}$. Instead, the dark count rate was initially as high as 0.015 counts $\text{pixel}^{-1}\ \text{s}^{-1}$, declining much more slowly than expected, as shown in Fig. 31.[63] The source of the dark count, namely phosphorescent window glow caused by impurities, is shown schematically in Fig. 32.[62] Measurements taken during a single day show that the dark count rate varies quadratically with

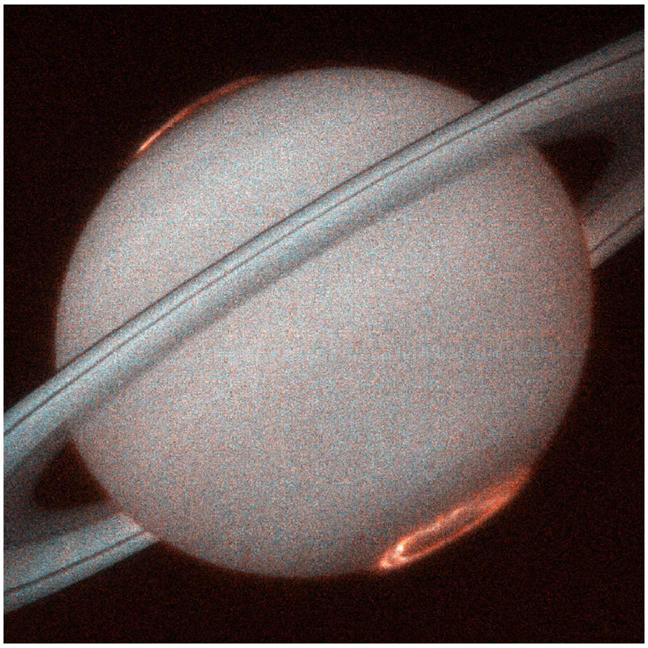

Fig. 28 Saturn's UV aurora. Composite image with molecular hydrogen color-coded blue, while Lyman-alpha emission is color-coded red.

temperature.[63] The overall dark count rate continues to slowly decline and is currently <0.002 counts $\text{pixel}^{-1}\ \text{s}^{-1}$ (see Fig. 33).[64]

Following the recovery of STIS, the FUV MAMA dark image had the same general appearance as in prior years.[65] The bright glow region (see Fig. 34) has a mean rate about a factor of 3 higher than the average for the whole detector. Typical overall dark count rates are 10^{-5} counts $\text{pixel}^{-1}\ \text{s}^{-1}$ at turn on, rising to $\sim 1.5 \times 10^{-5}$ counts $\text{pixel}^{-1}\ \text{s}^{-1}$ after several

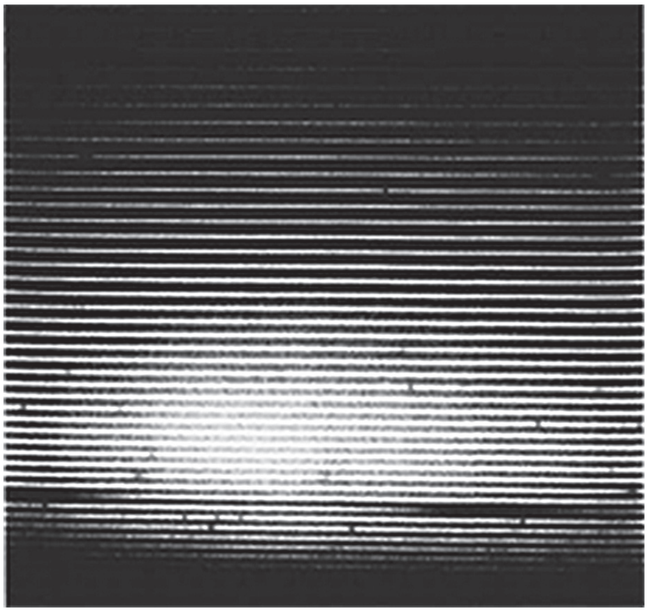

Fig. 29 Echelle spectrum of BD+28°4211. The spectrum covers the range from 115 to 170 nm with a nominal resolving power of 4.6×10^4. Broad Lyman alpha absorption is seen in two echelle orders near the bottom of the array format, along with numerous narrow stellar absorption lines.

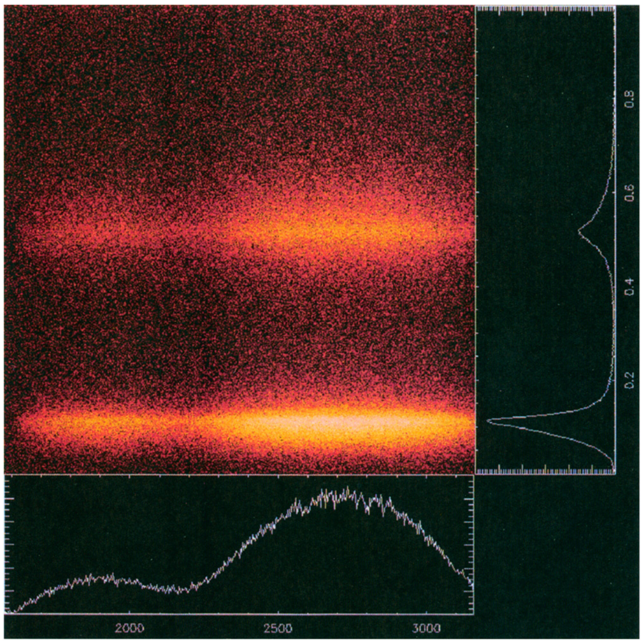

Fig. 30 Crab pulsar profile versus phase from 160 to 320 nm. The data do not indicate any wavelength dependence of the pulse profile (courtesy T. R. Gull et al., from Ref. 59).

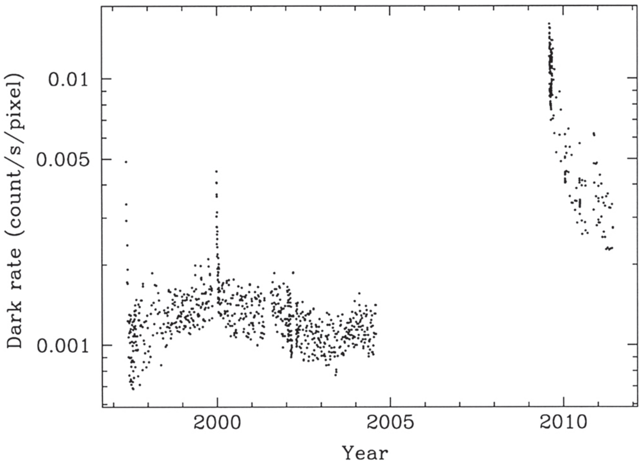

Fig. 31 History of the STIS NUV MAMA dark count rate (courtesy W. Zheng et al., from Ref. 63).

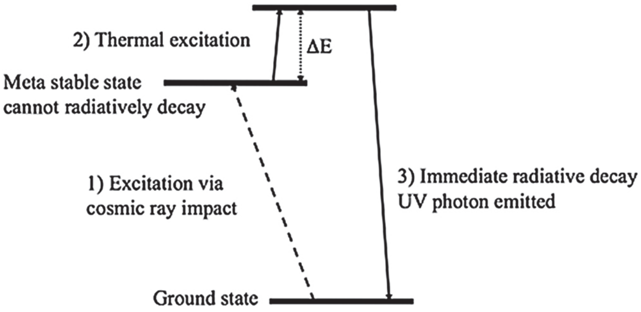

Fig. 32 Schematic representation of the source of the NUV MAMA dark count (courtesy C. R. Profitt et al., from Ref. 62).

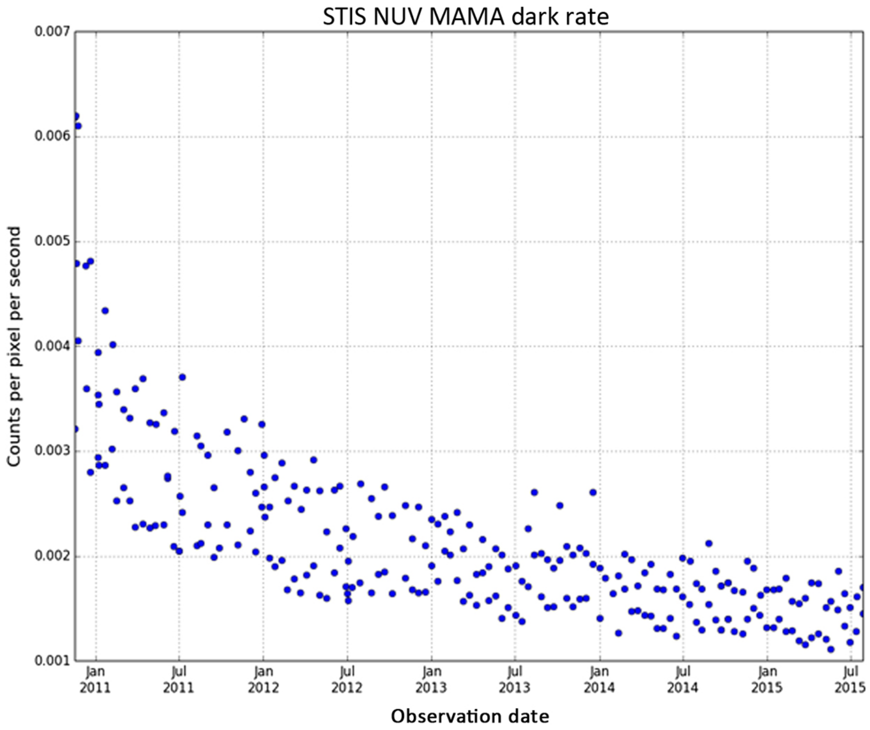

Fig. 33 STIS NUV MAMA dark count rate through July 2015 (courtesy STScI, from Ref. 64).

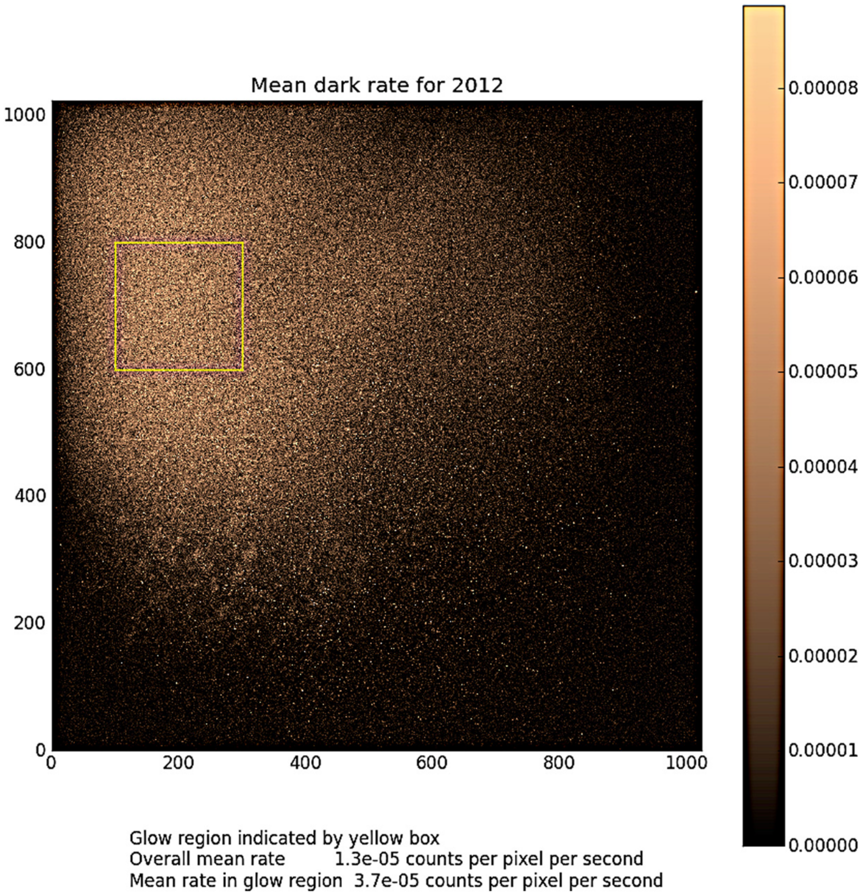

Fig. 34 STIS FUV MAMA dark count image in 2012 (courtesy C. Cox, Ref. 65).

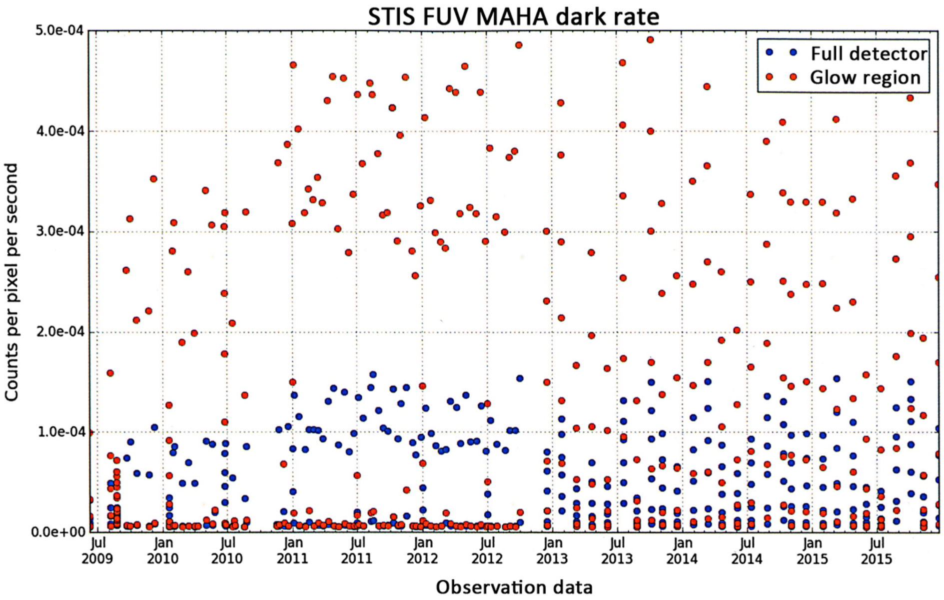

Fig. 35 STIS FUV MAMA dark count rate through July 2015 (courtesy STScI, from Ref. 64).

hours of operation. In the glow region, the rate rises to $\sim 4\times 10^{-5}$ counts pixel^{-1} s^{-1}. There is a significant variability in the ultimate dark count rate depending on the other activities on the HST and the intervening temperature profile.[65] The STIS FUV MAMA dark count rate remains highly variable, as shown in Fig. 35, but shows no significant trend through this date.[64]

The general health of both MAMAs remains excellent and there is no C-plate gain change apparent in the fold analysis histograms, as shown in Fig. 36.[66]

Further validating the stability of the STIS MAMAs is the CALSTIS calibration[67] using the CALSPEC standard stars. The weighted slope of the NUV MAMA sensitivity, expressed in stellar magnitudes, is −0.04 mmag year^{-1}, and the weighted slope of the FUV MAMA sensitivity is 0.54 mmag year^{-1}. This equates to sensitivity changes of <1.0 and 0.7%, respectively, over 15 years.[66] The CALSPEC flux standards are being consistently upgraded,[68] and CALSPEC can be considered in the general context of spectroradiometry with space telescopes.[69]

As examples of recent observations with the STIS FUV MAMA, we can consider the first detection of aurorae on Uranus and the motion of aurorae on Ganymede. The aurora on Uranus, as shown in Fig. 37, was discovered during active solar wind conditions.[70]

An image of the aurora on Ganymede is shown in Fig. 38. Measurements of the oscillations of the locations of the auroral ovals show that they are smaller than calculated, strongly suggesting the presence of an electrically conducting (i.e., saline) subsurface ocean.[71]

It is of note that the auroral images in Figs. 28 and 38 were taken ~12 years apart with the same detector system under identical operating conditions.

Both STIS MAMAs continue working well to this day.

3.3 *Advanced Camera for Surveys*

The flight-spare FUV MAMA detector was installed in the solar-blind channel (SBC) of the ACS (Ref. 72) during SM3B in March 2002. The SBC has an imaging area of 1024×1024 pixels with a sampling of 0.030 arc sec per pixel and a total field of view of $31\times 35\,(\mathrm{arcsec})^2$. The fold analysis showed little change in the distribution of charge over the period of about four years between ground testing and on-orbit operation. The MAMA is cosmetically reasonably clean with the only defects being a broken anode electrode and three small clusters of hot pixels.[73] The mean dark count was 3.9×10^{-5} counts pixel^{-1} s^{-1} at a tube temperature in the range of 15 to 27°C, with a rate of $\sim 1.1\times 10^{-2}$ counts pixel^{-1} s^{-1} in the bright central part of the dark image. The reference SBC dark image is shown in Fig. 39.[74]

The mean dark rate was remeasured in 2004 and found to be 1.0×10^{-5} counts pixel^{-1} s^{-1}, that is to say ~10 times less than that in the brightest part of the reference image.[75] The rate was measured again in 2008 and found to be unchanged for the first two hours of operation, after which it rose steadily by a factor of 2 to 3, due to a temperature effect (see Fig. 40).[76] The lower level is appropriate for most observations. No significant changes in efficiency of the MAMA have so far been observed.

In June 2006, ACS suffered an electronics failure, which was corrected by switching to the redundant side-2 electronics in July 2006. In January 2007, ACS failed again due to a short circuit in the backup power supply. The SBC was returned to operation in February 2007 using the side-1 electronics and, lightly used, continues working to this day.

3.4 *Cosmic Origins Spectrograph*

The COS instrument[77,78] was installed in HST on the fifth and final servicing mission SM4 in May 2009. The STIS flight-spare NUV MAMA was installed in the NUV channel. The NUV MAMA dark images are essentially featureless, as shown in Fig. 41,[79] with early measurements away from the SAA showing a rate of $\sim 6\times 10^{-5}$ counts pixel^{-1} s^{-1}. This was below the prelaunch predictions of $\sim 20\times 10^{-5}$ counts pixel^{-1} s^{-1}. However, the dark count rate rose steadily with time and stabilized at a level of $\sim 6\times 10^{-4}$ counts pixel^{-1} s^{-1} away from the SAA, as shown in Fig. 42.[80] The value of 8.6×10^{-4} counts pixel^{-1} s^{-1} was adopted, encompassing 95% of the observations in cycle 21. The fold analysis (see Fig. 43) shows highly stable operation of the MAMA through cycle 21.[80]

The COS FUV MAMA continues working well to this day.

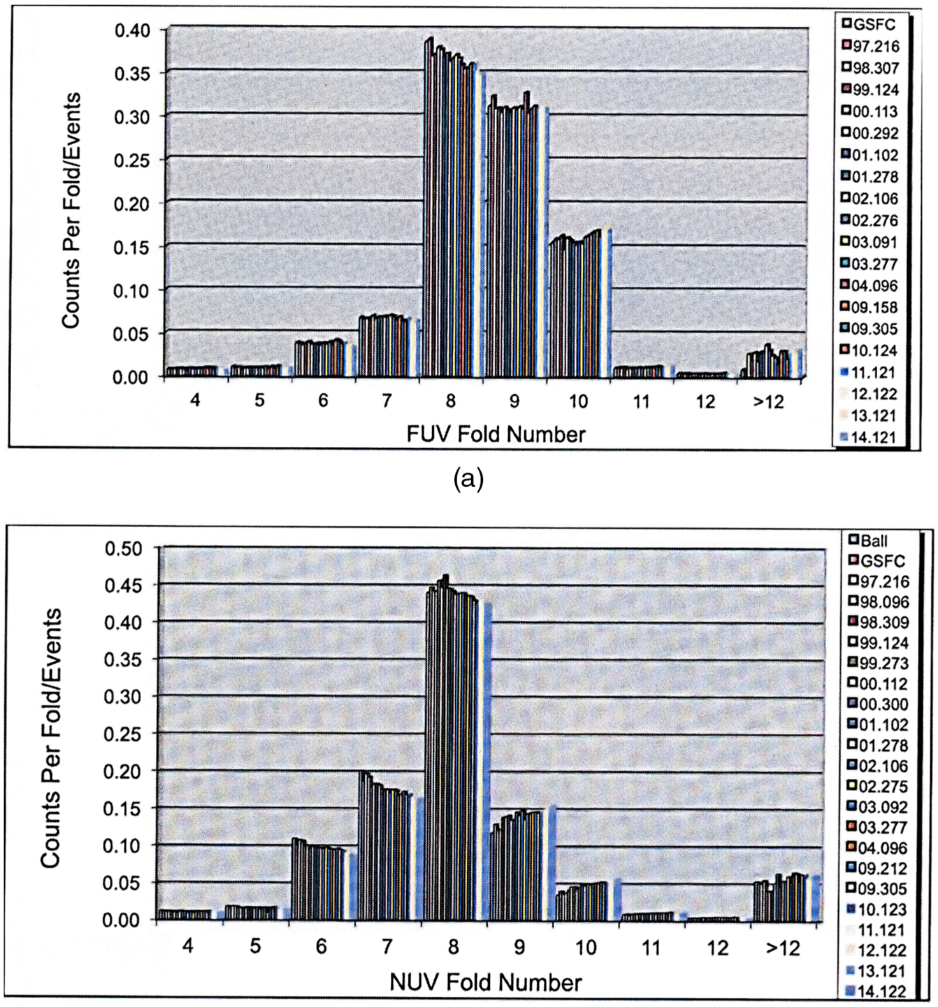

(a)

(b)

Fig. 36 STIS MAMA fold analyses through 2014 (courtesy H. Sana et al., from Ref. 66). Analyses are labeled by year and day number. (a) FUV MAMA. (b) NUV MAMA.

4 Lessons for Future Space Ultraviolet Astrophysics Missions

It is clear that the photoconductive arrays, such as the CCDs and CMOS sensors, are the prime candidate detectors for visible-light and near-infrared astrophysics missions. However, the wide-bandgap solar-blind photoconductive arrays for use in the UV are still in the early phases of development.[81]

The two STIS MAMAS have now been on orbit for almost 19 years, and working on orbit for almost 14.5 years. The ACS MAMA has now been working on orbit for nearly 14 years. The COS MAMA has now been working on orbit for about six years and nine months. The four HST MAMAs have now been working on orbit for a combined total of nearly 50 years without requiring any changes to the operating voltages or the electronics controls. This highly extended period of operation provides a number of lessons for the use of photoemissive detectors in future space UV astrophysics missions.

The requirements for photon-counting, large-format detectors for these forthcoming missions, particularly those devoted to spectroscopy, have recently been defined by NASA.[82] Specifically, arrays with high DQE (>50%), low noise per pixel ($<10^{-7}$ counts s^{-1}), large format ($>2000 \times 2000$ pixels), and operating at wavelengths from 100 to 400 nm or greater are required. It is clear from the on-orbit data that the MAMAs already meet some of these requirements, while further significant developments are needed in other areas.

First, given the correct operating conditions, the lead-glass MCPs are capable of meeting the requirements for future missions. This assumes that, for long-term space missions, it is possible to move the image or spectrum across the active area of the MCP in order to mitigate the effects of localized charge depletion by very bright spatial or spectral features. Given the finite amount of charge that can be extracted from the lead glass, the MAMAs provide the following critical characteristics from the MCP:

1. a required gain of 10^6 or less ($\sim 5 \times 10^5$ for the MAMA),
2. a maximum operating voltage of order 2000 V or less,
3. a single high-gain MCP, with highly effective suppression of ion feedback, to both improve the lifetime and to provide a small diameter of the output charge cloud to match the precision anode array readout.

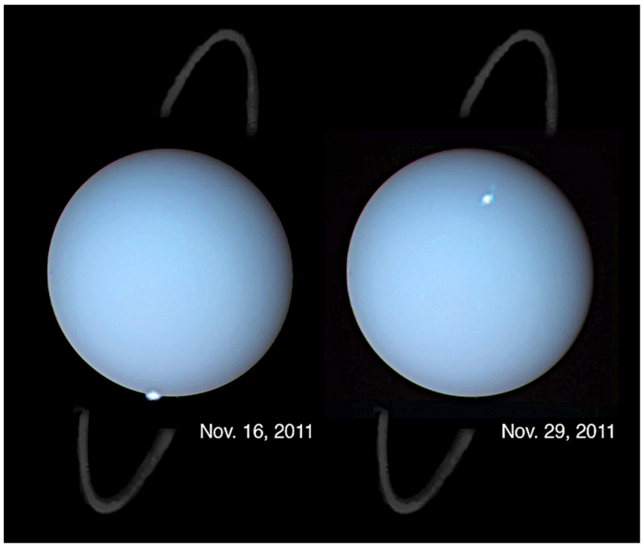

Fig. 37 Aurora on Uranus recorded with the STIS FUV MAMA. This composite image combines 2011 HST STIS observations of the aurorae in visible and ultraviolet light, 1986 Voyager 2 photos of the cyan disk of Uranus as seen in visible light, and 2011 Gemini Observatory observations of the faint ring system as seen in infrared light.[70]

Nevertheless, the limits on the local and global count rates for the MAMAs require stringent bright object limitations in order to protect the detectors from overillumination.[83] This limits the observing capabilities.

The C-plate provides a superior flat-field uniformity, a significantly higher dynamic range, and a longer lifetime than the Chevron or Z-stack MCPs. Further, the digital MAMA readout system provides many advantages over any of the current analog MCP readout systems. The performance of the MAMAs, particularly in high-resolution mode, could be significantly improved with the use of C-plates having 10-micron-diameter channels on 12-micron centers, or even 8-micron-diameter channels on 10-micron centers. If high-gain MCPs are required for future astrophysics missions, the development of C-plate fabrication processes, which can produce a number of plates simultaneously, reliably, and at commercially viable costs will clearly be needed. The Chevron and Z-stack MCPs simply cannot provide the flat-field uniformity and stability, the high SNR, the local dynamic range, or the lifetime for extended missions.

The amplifier and discriminator ASICs developed at Ball Aerospace and the decode ASICs developed at Stanford University have performed impeccably. However, given the major ongoing improvements in computer speed, a look-up table system may now offer speed and power improvements over the decode ASIC.

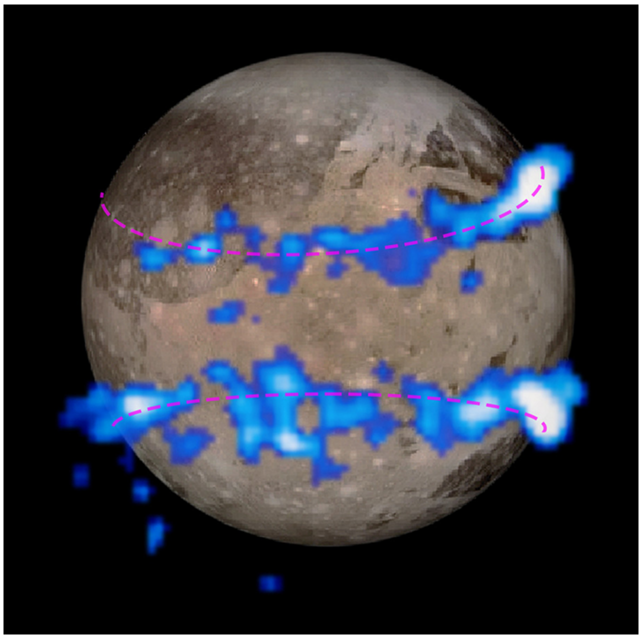

Fig. 38 Aurora on Ganymede recorded with the STIS FUV MAMA. The auroral belts are colored blue in this image and are overlaid on a visible-light image of Ganymede taken by NASA's Galileo orbiter.[71]

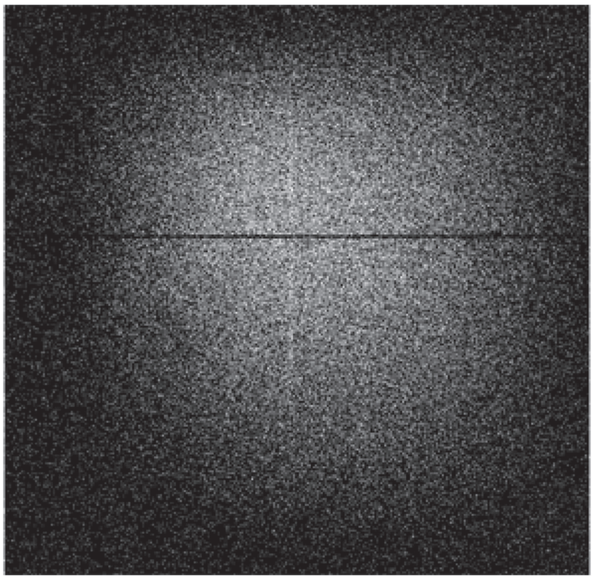

Fig. 39 SBC reference dark image (courtesy C. Cox, from Ref. 74).

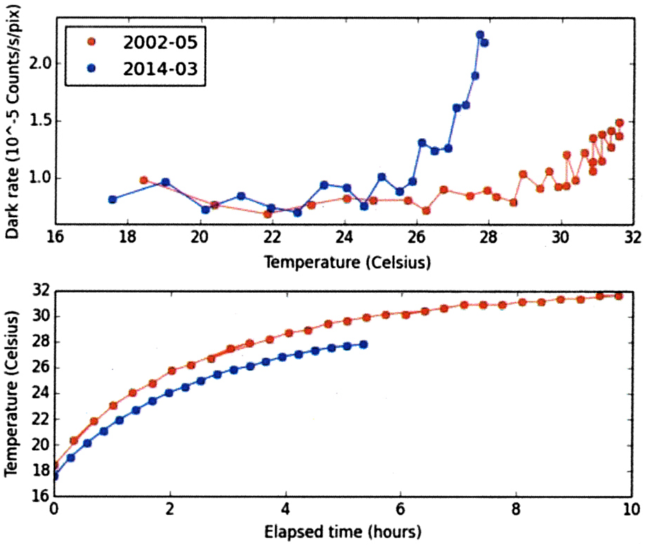

Fig. 40 ACS MAMA dark count rate as a function of the operating temperature (courtesy STScI, from Ref. 76).

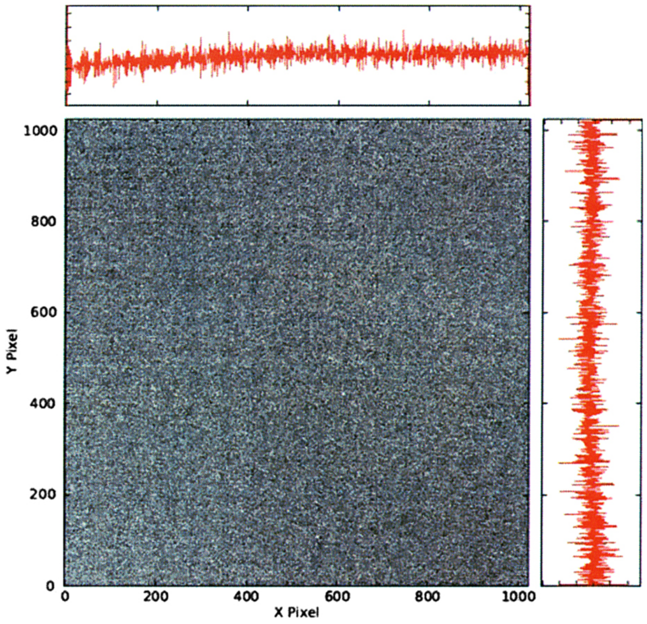

Fig. 41 COS NUV MAMA dark map (courtesy StSci, from Ref. 79).

The principal deficiencies of the MAMAs are the dark count rate and the photocathode quantum efficiency. First, the red leaks of both the FUV and the NUV MAMAS have increased significantly from the prelaunch values during on-orbit operation.[83] While the red leaks of the FUV MAMAs remain at tolerable levels, the red leaks of the NUV MAMAs are significantly above the desired levels for visible-light rejection. In many ways, this is not unexpected, as bare lead-glass CEMs and MCPs, which have a generally accepted work function on the order of 5 eV, routinely show a measurable response to laboratory fluorescent lights. The source of this contamination DQE is not, at present, well understood.

The dark count rate of the STIS NUV MAMA varies quadratically with temperature.[65] Clearly, more attention needs to be paid to the thermal control of the electronics and of the high- and low-voltage power supplies. However, the principal cause is probably the negative temperature coefficient of the lead-glass C-plate. The C-plate appears to be running hotter in space than in the laboratory because of the less desirable thermal environment. Recent developments have attempted to find a material superior to the lead glass for fabricating MCPs. The development of silicon-based MCPs has been pursued for some time;[84,85] however, it has not proved possible to obtain adequate gain from these MCPs, and the development appears not to be actively pursued at this time. Developments to produce aluminum oxide MCPs are also underway;[86] however, no working MCPs have yet been demonstrated.

The most promising development appears to be the production of resistive and secondary emission layers by an atomic layer deposition (ALD) process. ALD MCPs have been produced over conventional lead-glass MCPs[87] and also on borosilicate glass.[88] Gain and dark count rates appear to be very good, but lifetime data have yet to be measured in detail.

The key development area is that of producing stable high quantum efficiency solar-blind photocathode materials. At FUV wavelengths, the most obvious upgrade is to make the MgF_2 window removable, as has been successfully implemented with the COS FUV detector. This, of course, would require changes to the MCP active area geometry, as has been successfully implemented for the SOHO C-plates. However, at this time, opaque CsI remains the best FUV photocathode material for use at wavelengths below ~160 nm. The situation at NUV wavelengths is much more complex. The most promising NUV photocathode material at this time is p-doped GaN.[89–91] The

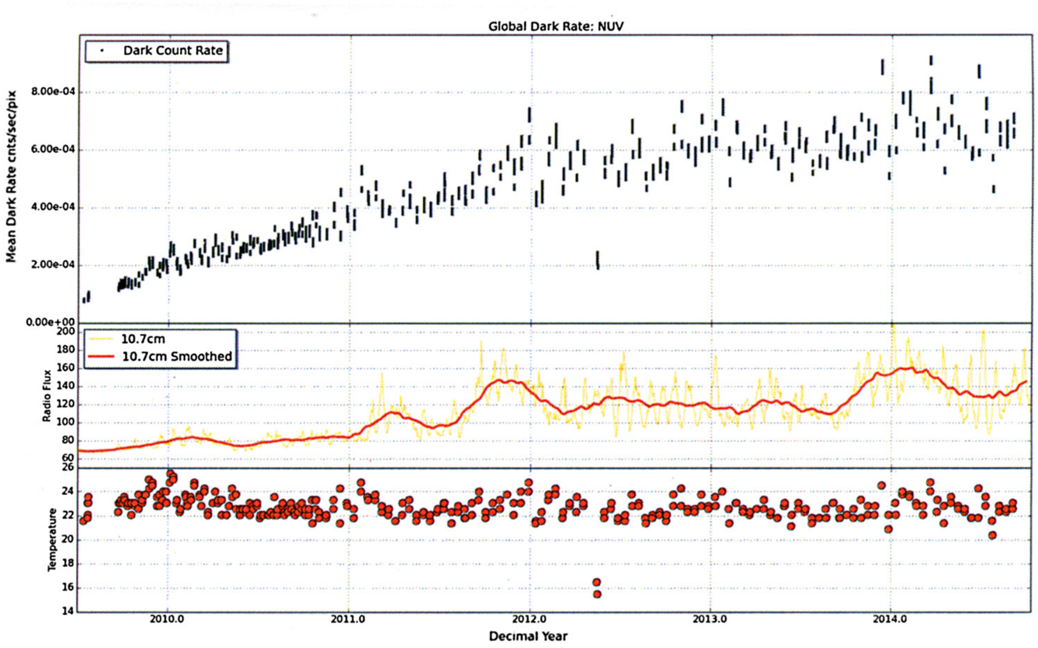

Fig. 42 COS NUV MAMA dark count rate as a function of time through Cycle 24. The first subplot shows the measured dark-rate in 25 s increments throughout every observation. The middle subplot displays the 10.7-cm radio flux used to track the solar cycle, and the last subplot displays the MAMA temperature for each observation (courtesy H. Sana et al., from Ref. 80).

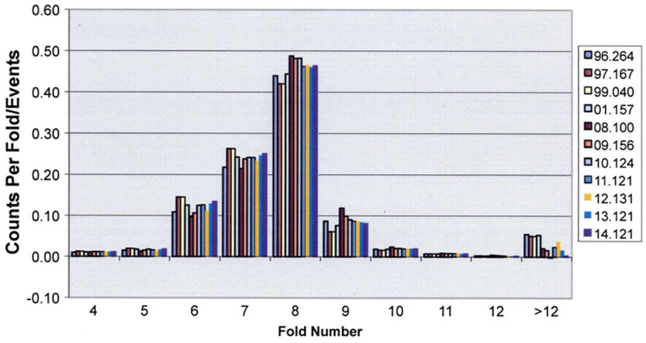

Fig. 43 COS NUV MAMA fold analysis through Cycle 21 (courtesy H. Sana et al., Ref. 80). Analyses are labeled by year and day number.

highest quantum efficiencies are produced by opaque photocathodes, which require cesium activation. It will accordingly be extremely difficult to combine these with current MCPs.

Whatever the results of these developments, there will always be a requirement in UV astrophysics instruments for photoconductive or photoemissive solar-blind imaging detector systems that are radiation tolerant and do not require cryogenic cooling.

In many ways, HST represents the very highly successful conclusion of the first phase of space astrophysics, which started at Peenemünde in Germany in 1944 and emphasized studies at high photon energies in the UV, x-ray, and gamma ray spectral regions.[92] Space observations at visible-light and infrared wavelengths were slower to get started, except for solar studies, because of the early conservative approach by a number of astronomers, e.g., the cost of "six Palomars vs one space telescope."[93] However, those early days are now long gone and the value of space telescopes in all wavelength ranges is universally accepted. The next phase will start by emphasizing the infrared with the James Web Space Telescope[94] and the Wide Field Infrared Survey Telescope.[95] Following these infrared missions, studies of concepts for large ultraviolet, optical, and infrared[96] space telescopes are now beginning, such as the Advanced Technology Large-Aperture Space Telescope.[97] Those advanced missions will once again require state-of-the-art, photon-counting, solar-blind imaging sensor technologies building on the lessons learned from the first-generation telescopes and instruments.

5 Conclusion

The STIS MAMAs have met all of the fundamental requirements for solar-blind imaging, high-resolution UV spectroscopy, and time-tag imaging, and, like most of the STIS components, have considerably exceeded the design life of five years. In addition, the flight-spare MAMAs have added considerably to the capabilities of the ACS and COS instruments. Based on the recent measurements of the performance characteristics, all of the MAMAs continue to work well and, in the absence of any unexpected random failures, may well continue to operate for the lifetime of HST.

The cumulative total of nearly 50 years of on-orbit operation for the two FUV MAMAs and the two NUV MAMAs over a 19-year period provides a substantial quantitative database from which to start the development of the next generation of photon-counting, solar-blind detector arrays for future space UV astrophysics missions.

Acknowledgments

I am very happy to acknowledge the invaluable contributions of all the individuals, unfortunately too many to mention by name, in academia, government, and industry (particularly at the prime contractor Ball Aerospace) who were critical to the success of STIS and the MAMAs. I am also grateful to all at STScI who were so helpful to me in providing essential data for this review and to the reviewers for their helpful and constructive comments and suggestions. This work was supported by the National Science Foundation and NASA with grants and contracts to the Harvard College Observatory, the University of Colorado, and Stanford University, and by NASA with contracts to Ball Aerospace. This paper is dedicated to the memory of my long-time friend and colleague Bruce Woodgate, without whose patience and dedication STIS and the MAMAs could never have come to fruition.

References

1. J. G. Timothy and R. L. Bybee, "Multi-anode microchannel arrays," *Proc. SPIE* **0116**, 24 (1977).
2. J. G. Timothy, G. H. Mount, and R. L. Bybee, "Detector arrays for photometric measurements at soft x-ray, ultraviolet and visible wavelengths," *Proc. SPIE* **0183**, 169 (1979).
3. J. G. Timothy et al., "MAMA detector systems: a status report," *Proc. SPIE* **1158**, 104 (1989).
4. B. E. Woodgate et al., "The space telescope imaging spectrograph design," *Publ. Astron. Soc. Pacific* **110**, 1183 (1998).
5. J. L. Wiza, "Microchannel plate detectors," *Nucl. Instrum. Methods* **162**, 587 (1979).
6. J. G. Timothy, "Microchannel plates for photon detection and imaging in space," in *Observing Photons in Space*, M. C. E. Huber et al., Eds., p. 365, International Space Science Institute, Bern, Switzerland (2010).
7. J. G. Timothy, "Microchannel plates for photon detection and imaging in space," in *Observing Photons in Space—A Guide to Experimental Space Astronomy*, 2nd ed., M. C. E. Huber et al., Eds., p. 391, Springer, New York (2013).
8. O. H. W. Siegmund et al., "Microchannel plates for the UVCS and SUMER instruments on the SOHO satellite," *Proc. SPIE* **2518**, 344 (1995).
9. A. S. Tremsin et al., "Electronic and optical moiré interference with microchannel plates," *Appl. Opt.* **38**, 2240 (1999).
10. J. B. McPhate et al., "Cosmic origins spectrograph FUV detector," *Proc. SPIE* **4139**, 25 (2000).
11. J. V. Vallerga et al., "HST-COS far-ultraviolet detector: final ground calibration," *Proc. SPIE* **4498**, 141 (2001).
12. A. S. Tremsin, J. V. Vallerga, and O. H. W. Siegmund, "Detector walk in position-sensitive detectors with biased microchannel plates," *Rev. Sci. Instrum.* **71**, 3758 (2000).
13. D. J. Sahnow et al., "Gain sag in the FUV detector of the cosmic origins spectrograph," *Proc. SPIE* **8145**, 81450Q (2011).
14. K. Wilhelm et al., "First results of the SUMER telescope and spectrometer on SOHO," *Solar Phys.* **170**, 75 (1997).
15. J. G. Timothy, "Curved-channel microchannel array plates," *Rev. Sci. Instrum.* **52**, 1131–1142 (1981).
16. D. C. Slater et al., "Imaging MAMA detector systems," *Proc. SPIE* **1243**, 35 (1990).
17. M. Corbett et al., "Development efforts to improve curved-channel microchannel plates," *Proc. SPIE* **1764**, 240 (1992).
18. J. P. Boutot et al., "A microchannel plate with curved channels: an improvement in gain, relative variance and ion noise for channel plate tubes," in *Proc. Sixth Symp. on Photo-electronic Image Devices*, p. 103, London (1974).
19. J. G. Timothy et al., "Performance characteristics of the MAMA detectors for the SUMER instrument on the SOHO mission," *Proc. SPIE* **2006**, 69 (1993).
20. J. G. Timothy et al., "MAMA detector systems: a status report," *Proc. SPIE* **1158**, 104 (1989).
21. J. G. Timothy, "Microchannel plates and image detection at soft x-ray wavelengths," *Proc. SPIE* **0597**, 330 (1986).

22. D. C. Slater and J. G. Timothy, "Microchannel plate modal gain variations with temperature," *Rev. Sci. Instrum.* **64**, 430 (1993).
23. V. S. Argabright et al., "Photometric stability of the STIS MAMA detectors," *Proc. SPIE* **3356**, 389 (1998).
24. C. L. Joseph et al., "Performance results of the STIS flight MAMA detectors," *Proc. SPIE* **2551**, 248 (1995).
25. B. N. Laprade and S. T. Reinhart, "Recent advances in small pore microchannel plate technology," *Proc. SPIE* **1072**, 119 (1989).
26. J. S. Morgan et al., "Position sensitivity of MAMA detectors," *Proc. SPIE* **0932**, 236 (1988).
27. J. S. Morgan et al., "Centroid position measurements and subpixel sensitivity variations with the MAMA detector," *Appl. Opt.* **28**, 1178 (1989).
28. D. B. Kasle and E. P. Horch, "Performance of high resolution decoding with multi-anode microchannel array detectors," *Proc. SPIE* **1764**, 202 (1993).
29. H. Ferguson, M. Clampin, and V Argabright, "Cycle7 MAMA pulse height distribution stability: fold analysis measurement," Instrument Science Report STIS 98–02R, Space Telescope Science Institute, Baltimore, Maryland (1998).
30. O. H. W. Siegmund et al., "Extreme ultraviolet quantum efficiency of opaque alkali halide photocathodes on microchannel plates," *Proc. SPIE* **0868**, 18 (1988).
31. A. S. Tremsin and O. H. W. Siegmund, "The quantum efficiency and stability of UV and soft x-ray photocathodes," *Proc. SPIE* **5920**, 1 (2005).
32. Space Telescope Imaging Spectrograph Instrument Handbook for Cycle 24, Version 15.0, Space Telescope Science Institute, Baltimore, Maryland, www.stsci.edu/hst/stis/documents/handbooks (2016).
33. A. H. Sommer, *Photoemissive Materials*, Robert E. Krieger Publishing Company, Huntington, New York (1980).
34. C. L. Joseph et al., "Performance results of the STIS flight MAMA detectors," *Proc. SPIE* **2551**, 248 (1995).
35. E. H. Cole and L. G. Smeins, "Signal processing for MAMA detector readout," *Proc. SPIE* **1158**, 183 (1989).
36. E. H. Cole and L. G. Smeins, "Monolithic integrated-circuit charge amplifier and comparator for MAMA readout," *Proc. SPIE* **1549**, 46 (1991).
37. L. G. Smeins, J. M. Stechman, and E. H. Cole, "An application-specific integrated-circuit-based multi-anode microchannel array readout system," *Proc. SPIE* **1549**, 59 (1991).
38. E. H. Cole, L. G. Smeins, and J. M. Stechman, "STIS ASIC charge-amp and voltage discriminator for MAMA detector readout," *Proc. SPIE* **1952**, 329 (1993).
39. E. H. Cole et al., "Space telescope imaging spectrometer 1K by 1K MAMA detector charge amplifier and discriminator flight electronics performance," *Proc. SPIE* **2551**, 239 (1995).
40. D. B. Kasle, "An ASIC for high speed and high resolution decoding of multi-anode microchannel array detectors," PhD Dissertation, Department of Electrical Engineering, Stanford University (1992).
41. D. B. Kasle and G. De Micheli, "An image decoding ASIC for spaced-based applications," in *Proc. Euro ASIC*, pp. 86–91 (1991).
42. J. G. Timothy and J. S. Morgan, "Imaging by time-tagging photons with the multi-anode microchannel array detector system," *Proc. SPIE* **0627**, 654 (1986).
43. G. Giaretta et al., "Time-tag photon detection with the MAMA detector system," *Proc. SPIE* **1952**, 316 (1993).
44. E. Horch et al., "A new speckle interferometry system for the MAMA detector," *Publ. Astron. Soc. Pacific* **104**, 939 (1992).
45. E. Horch et al., "Speckle observations of binary stars with the WIYN telescope. I. Measures during 1997," *Astron. J.* **117**, 548 (1999).
46. E. Horch et al., "Speckle interferometry of southern double stars. II. Measures from the Casleo 2.15 meter telescope, 1995–1996," *Astron. J.* **121**, 1597 (2001).
47. J. S. Morgan et al., "High time-resolution imaging with the MAMA detector systems," *Proc. SPIE* **1235**, 347 (1990).
48. A. M. Smith et al., "Far-ultraviolet MAMA detector imagery and emission-line CCD imagery of NGC 6240," *Astron. J.* **391**, L81 (1992).
49. C. L. Joseph et al., "Test and evaluation of the STIS engineering model units of the MAMA detectors," *Proc. SPIE* **2282**, 116 (1994).
50. V. S. Argabright et al., "Photometric stability of STIS MAMA detectors," *Proc. SPIE* **3356**, 389 (1998).
51. R. A. Kimble, "The on-orbit performance of the STIS detectors," in *1997 HST Calibration Workshop*, p. 8 (1997).
52. R. A. Kimble et al., "In-flight performance of the MAMA detectors on the space telescope imaging spectrograph," *Proc. SPIE* **3764**, 209 (1999).
53. R. A. Kimble et al., "The on-orbit performance of the space telescope imaging spectrograph," *Astrophys. J.* **492**, L83 (1998).
54. M. E. Kaiser et al., "Space telescope imaging spectrograph detectors and ultraviolet signal-to-noise capabilities," *Proc. SPIE* **3356**, 415 (1998).
55. R. L. Gilliland, "Use of FP-SPLIT slits for reaching high signal-to-noise with MAMA detectors," Instrument Science Report STIS 98–16, Space Telescope Science Institute, Baltimore, Maryland (1998).
56. J. T. Trauger, "Saturn's ultraviolet aurora," STScI-1998-05, Space Telescope Science Institute, Baltimore, Maryland (1998).
57. R. A. Kimble et al., "The on-orbit performance of the space telescope imaging spectrograph," *Proc. SPIE* **3356**, 188 (1998).
58. E. B. Jenkins et al., "Ultraviolet absorption lines from high-velocity gas in the vela supernova remnant: new insights from space telescope imaging spectrograph echelle observation of HD 72089," *Astrophys. J.* **492**, L147 (1998).
59. T. R. Gull et al., "Space telescope imaging spectrograph near-ultraviolet time-tagged spectra of the crab pulsar," *Astrophys. J.* **495**, L51 (1998).
60. C. R. Proffitt et al., "STIS calibration status," in *2002 HST Calibration Workshop*, p. 97 (2002).
61. S. A. Rinehart et al., "Technical aspects of the space telescope imaging spectrograph repair (STIS-R)," *Proc. SPIE* **7010**, 70104R (2008).
62. C. R. Proffitt et al., "Performance of the space telescope imaging spectrograph after SM4," in *2010 HST Calibration Workshop*, p. 47 (2010).
63. W. Zheng, C. Proffitt, and D. Sahnow, "Dark rate of the STIS NUV detector," Instrument Science Report STIS 2011–03, Space Telescope Science Institute, Baltimore, Maryland (2011).
64. STScI, *STIS Monitoring* (2016).
65. C. Cox, "Dark count rates in the STIS MAMA," Instrument Science Report STIS 2015–07, Space Telescope Science Institute, Baltimore, Maryland (2015).
66. H. Sana et al., "Summary of the STIS cycle 21 calibration program," Instrument Science Report STIS 2015–09, Space Telescope Science Institute, Baltimore, Maryland (2015).
67. STIS, *Instrument Handbook for Cycle 24*, Space Telescope Science Institute, Baltimore, Maryland (2015).
68. R. C. Bohlin, "Hubble Space Telescope CALSPEC flux standards: SIRIUS (AND VEGA)," *Astron. J.* **147**, 127 (2014).
69. A. Pauluhn et al., "Spectroradiometry with space telescopes," *Astron. Astrophys. Rev.* **24**, 3 (2016).
70. L. Lamy et al., "Earth-based detection of Uranus' aurorae," *Geophys. Res. Lett.* **39**, L07105 (2012).
71. J. Saur et al., "The search for a subsurface ocean in Ganymede with Hubble Space Telescope observations of its auroral ovals," *J. Geophys. Res.* **120**, 1715 (2015).
72. H. Ford et al., "The advanced camera for the Hubble Space Telescope," *Proc. SPIE* **3356**, 234 (1998).
73. H. D. Tran et al., "On-orbit performance of the ACS solar blind channel," in *2002 HST Calibration Workshop*, p. 86 (2002).
74. C. Cox, "SBC dark and cumulative images," Instrument Science Report ACS 2004–014, Space Telescope Science Institute, Baltimore, Maryland (2004).
75. C. Cox, "Re-measurement of ACS/SBC dark images," Instrument Science Report ACS 2009–02, Space Telescope Science Institute, Baltimore, Maryland (2009).
76. STScI, *ACS Instrument Handbook for Cycle 24*, Space Telescope Science Institute, Baltimore, Maryland (2016).
77. J. C. Green, "The comic origins spectrograph," *Proc. SPIE* **4498**, 229 (2001).
78. A. Aloisi et al., "The on-orbit performance of the cosmic origins spectrograph," in *2010 HST Calibration Workshop*, p. 11 (2010).
79. STScI, *COS Instrument Handbook for Cycle 24*, Space Telescope Science Institute, Baltimore, Maryland (2016).
80. H. Sana et al., "Summary of COS cycle 21 calibration program," Instrument Science Report COS 2015–06, Space Telescope Science Institute, Baltimore, Maryland (2015).

81. U. Schühle and J.-F. François Hochendez, "Solar-blind UV detectors based on wide band gap semiconductors," in *Observing Photons in Space—A Guide to Experimental Space Astronomy*, 2nd ed., M. C. E. Huber et al., Eds., p. 467, Springer, New York (2013).
82. Cosmic Origins, NASA Goddard Space Flight Center, Greenbelt Maryland, http://cor.gsfc.nasa.gov/technology/ (2016).
83. STIS, *Instrument Handbook for Cycle 24*, Space Telescope Science Institute, Baltimore, Maryland (2016).
84. O. H. W. Siegmund et al., "Next generation microchannel plate detector technologies for UV astronomy," *Proc. SPIE* **5488**, 789 (2004).
85. A. S. Tremsin et al., "Thermal dependence of electrical characteristics of micromachined silica microchannel plates," *Rev. Sci. Instrum.* **75**, 1068 (2004).
86. G. Drobychev et al., "Advances in anodic alumina MCP development," *Nucl. Instrum. Methods Phys. Res. Sect. A* **610**, 246 (2009).
87. D. R. Beaulieu et al., "Nano-engineered ultra-high-gain-microchannel plates," *Nucl. Instrum. Methods Phys. Res. Sect. A* **607**, 81 (2009).
88. O. H. W. Siegmund et al., "Atomic layer deposited borosilicate glass microchannel plates for large area event counting detectors," *Nucl. Instrum. Methods Phys. Res. Sect. A* **695**, 168 (2012).
89. J. Stock et al., "Progress on development of UV photocathodes for photon-counting applications at NASA GSFC," *Proc. SPIE* **5898**, 58980F (2005).
90. Q. Yunsheng et al., "Activation and evaluation of GaN photocathodes," *Proc. SPIE* **7481**, 74810H (2009).
91. O. H. W. Siegmund et al., "Gallium nitride photocathodes for imaging photon counters," *Proc. SPIE* **7732**, 77324T (2010).
92. M. C. E. Huber, A. Pauluhn, and J. G. Timothy, "Observing photons in space," in *Observing Photons in Space—A Guide to Experimental Space Astronomy*, 2nd ed., Vol. **1**, M. C. E. Huber et al., Eds., Springer, New York (2013).
93. E. Stuhlinger, "Enabling technology for space transportation," in *The Century of Space Science*, Vol. **1**, J. A. M. Bleeker, J. Geiss, and M. C. E. Huber, Eds., p. 59, Springer, The Netherlands (2001).
94. James Webb Space Telescope (JWST), NASA, www.jwst.nasa.gov/ (2016).
95. Wide Field Infrared Survey Telescope, NASA, www.stsci.edu/wfirst (2016).
96. J. Tumlinson et al., "Beyond JWST: science drivers for the next great UVOIR space telescope," presented at *American Astronomical Society Meeting #225, #338.19*, Space Telescope Science Institute, Baltimore, Maryland (2015).
97. Advanced Technology Large-Aperture Space Telescope, Space Telescope Science Institute, Baltimore, Maryland, www.stsci.edu (2016).

J. Gethyn Timothy received the PhD degree from University College London in 1971 and the DSc degree from the University of London in 2004. He remains fascinated by all aspects of low-light-level imaging and spectroscopy, particularly at ultraviolet and extreme-ultraviolet wavelengths, while enjoying the relaxation of time afforded by retirement.